POLITECNICO DI TORINO
Repository ISTITUZIONALE

A comprehensive formalism for air-gap membrane distillation applied to the design of full-scale modules with direct solar heating

Original
A comprehensive formalism for air-gap membrane distillation applied to the design of full-scale modules with direct solar heating / Lesniewska, N., Morciano, M., Tiraferri, A., Fasano, M.. - In: DESALINATION. - ISSN 0011-9164. - 622:(2026). [10.1016/j.desal.2025.119700]

Availability:
This version is available at: 11583/3006090 since: 2025-12-22T11:19:11Z

Publisher:
Elsevier

Published
DOI:10.1016/j.desal.2025.119700

Terms of use:

This article is made available under terms and conditions as specified in the corresponding bibliographic description in the repository

Publisher copyright

(Article begins on next page)

15 November 2026

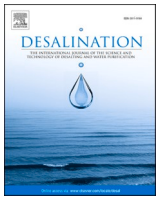
Desalination 622 (2026) 119700



Contents lists available at ScienceDirect

Desalination

journal homepage: www.elsevier.com/locate/desal



A comprehensive formalism for air-gap membrane distillation applied to the design of full-scale modules with direct solar heating

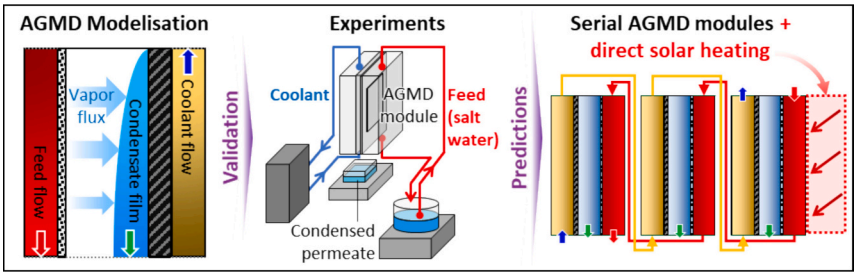
Nicolas Lesniewska [a], Matteo Morciano [b], Alberto Tiraferri [a], Matteo Fasano [b,*]

[a] Department of Environment, Land and Infrastructure Engineering (DIATI), Politecnico di Torino, Corso Duca degli Abruzzi 24, 10129, Turin, Italy
[b] Department of Energy (DENERG), Politecnico di Torino, Corso Duca degli Abruzzi 24, 10129, Turin, Italy

HIGHLIGHTS

- CFD model couples heat, mass, fluid transport within improved AGMD formalism
- Model validated with seawater AGMD experiments at feed temperature up to 60 °C
- Optimal AGMD module design strongly depends on assembly (single vs. multi-module)
- Assessed productivity of a full-scale system of 3 series-connected AGMD modules
- Direct solar heating increases AGMD full-scale system productivity up to 230 %

GRAPHICAL ABSTRACT



ARTICLE INFO

Keywords:
Desalination
Air-gap membrane distillation
Module design
Solar energy
Computational fluid dynamics

ABSTRACT

Air-gap membrane distillation (AGMD) is used to extract volatile compounds from a heated feed solution, through a porous hydrophobic membrane, into a cooled compartment, then recovered by condensation. AGMD is a promising technology for desalination and aqueous concentration, but its scale-up is limited by incomplete physical descriptions of the module physics. This work proposes a new CFD-based multiphysics framework to design AGMD full-scale plate-and-frame modules for freshwater extraction. The three physics features comprised within an AGMD module are first formalized: (i) the flow of a solution in contact with a porous membrane; (ii) gas mixture (vapor) transport through a porous membrane; (iii) vapor condensation on a (vertical) surface. They are thus combined into a consistent formalism of the AGMD module physics, with a particular focus on gas transport built upon the Maxwell-Stefan theory, which is here improved to account for medium vapor saturation. Model predictions are validated experimentally against lab-scale AGMD data for feed temperature up to 60 °C. The model is then employed to assess full-scale flat-sheet modules, connected in series, and enhanced with direct solar heating. Simulations reveal that system productivity is highly sensitive to configuration (single vs. multi-module; bulk solar vs. direct solar heating), with optimal productivity achieved with considerably different module compartment design and process parameters. When enhanced with direct solar heating, system optimal productivity can increase by up to 230 % compared to standard configurations. This formalism provides a robust basis for AGMD modules design and prior to their effective integration into real-world desalination system.

* Corresponding author.
E-mail addresses: nicolas.lesniewska@polito.it (N. Lesniewska), alberto.tiraferri@polito.it (A. Tiraferri), matteo.fasano@polito.it (M. Fasano).

https://doi.org/10.1016/j.desal.2025.119700
Received 1 October 2025; Received in revised form 27 November 2025; Accepted 29 November 2025
Available online 30 November 2025
0011-9164/© 2025 The Authors. Published by Elsevier B.V. This is an open access article under the CC BY license (http://creativecommons.org/licenses/by/4.0/).

1. Introduction

Freshwater scarcity is a worsening problem affecting billions of people [1,2], which prompts a paradigm shift into the management of vital water resources alongside the development of innovative technical solutions for wastewater treatment [3], groundwater use [4] or water storage [5], to quote a few. Among the explored solutions [6], desalination processes make it feasible to exploit high-salinity solutions including seawater, which is arguably the most abundant and available source of water on the Earth's surface. However, desalination methods (e.g. via distillation) [7,8] are sometimes considered inefficient in terms of salt separation rates and energy needs, difficult to implement on a large scale and/or economically challenging [9]. Moreover, concerns are growing about the environmental footprint of desalination, and therefore an increasing number of studies investigate the use of sustainable energy sources (e.g., solar energy) for water treatment [10]. Meanwhile, in the field of desalination, membrane-based technologies are gradually gaining ground, as they emerge as efficient, sustainable, and promising processes for water purification, among other uses (e.g. brine extraction) [11,12].

Membrane distillation (MD) is a separation process that uses a hydrophobic porous membrane to extract volatile compounds from a liquid feed stream while preventing liquid phase from passing through [13,14]. Permeation of volatile compounds is generally induced by a vapor pressure difference created by an imposed temperature or pressure gradient, concentration gradient (e.g., osmotic pressure difference), or even by an electric field applied across the membrane [15–18]. MD technologies are therefore well suited to desalination and water purification, as they can notably offer high salt and non-volatile contaminant retention rates, with extensive number of works proposing improvements in their technical, economic, and environmental efficiency [19,20]. Representative MD configurations include direct contact membrane distillation (DCMD) modules, where permeation occurs from a heated feed liquid stream, through the membrane, into a cooled permeate liquid stream [21,22]. Improving the classical DCMD process, air-gap membrane distillation (AGMD) systems extract volatile compounds (e.g. water vapor) from the liquid feed through a (micro)porous membrane into a chamber containing a stagnant gas, with the permeate recovered via an integrated (or associated) condensation process [23,24]. Compared to a DCMD module, the gas gap between feed and cooling channel in AGMD should improve the thermal efficiency of the process by reducing the temperature polarization effect, which then allows to work at a lower feed temperature while maintaining a relevant permeate production rate [25,26].

In line with previous concerns, this work proposes a new comprehensive model to assess and optimize the performance of AGMD processes by specifically focusing on the core module physics, with the view of developing large-scale modules suitable for real-scale uses, such as wastewater treatment or desalination. As a starting point for module development, a large number of previous works propose models of AGMD physics, often relying on laboratory-scale experiments to calibrate and evaluate their predictions over a range of operating conditions (e.g., temperature, feed solution velocity, density) [27–32]. Most of these recent works apply a similar theoretical approach to formalize heat and mass transfer in an AGMD, which is essential for predicting the efficiency of a potential module – i.e., permeate production versus energy consumption –, making extensive use of analytical approximations to express the fluxes (e.g., using an analogy of a thermal resistance-equivalent circuit). These approximations consist mostly in considering the liquid and gaseous phases within an AGMD module as media with isotropic properties, which gives satisfactory predictions for small-scale modules and/or operating conditions involving often relatively small temperature gradients throughout the module (cf. e.g. [26]). Consequently, designing a module at the pilot or real scale [33] or with innovative operation (e.g., with passive flows [34]) necessarily involves tackling the limitations of the aforementioned standard models, and thereby revisiting the physics of AGMD processes.

An AGMD system can be modelled as the convolution of three physical processes: the flow of a solution in contact with a porous wall [35,36]; the transport of gas (vapor) through a porous media [37,38]; the water vapor condensation on a (vertical) wall [39,40]. These three features are still the subject of active research and need to be treated with care when they are interwoven to describe the complex physics of large-scale AGMD systems, especially wherever usual approximations would not hold (e.g., linear variation of the temperature throughout a module [33,34,41]). For the sake of exemplification, recent studies discuss the advantage of considering dropwise condensation as a more appropriate and/or desired mechanism for collecting permeate in an AGMD system, instead of or in conjunction with filmwise condensation on a cooling plate surface (module-internal condenser) [40,42]. Overall, to address the AGMD multiphysics, it is necessary to handle an analytical formalism that requires the use of advanced numerical methods to provide accurate projections about module efficiency as a function of its configuration and operating conditions [43,44].

In this work, the authors introduce a comprehensive multiphysics formalism for AGMD that unifies the description of heat flux, liquid flow, vapor transport, and condensation within a single framework. Unlike conventional models that rely on simplified analytical approximations [27], this approach explicitly resolves the coupled heat and mass transfer equations with complete spatial discretization of AGMD module physics, extending from classical formulations [13,45] to incorporate advanced effects, such as the Soret contribution (thermodiffusion) [46] and medium vapor saturation constraints [47]. Theoretical developments first address the physics of an AGMD module in a general way, so that it can be transposed to various feed, coolant and gas phases compositions, and different module dimensions, thereby providing a basis for future studies on MD processes of interest.

In the scope of this work, the new theoretical framework is applied to the specific case of pure water extraction from a seawater feed solution via AGMD. In particular, the CFD model is used to predict permeate production from the scale of a laboratory AGMD module, to that of potential large-scale implementations. Experiments on water purification with a standard laboratory-scale AGMD module are carried out to evaluate the CFD model accuracy and highlight its limitations. The authors explore different AGMD module dimensions and operating conditions (feed and coolant velocity, temperature, salt density), to sort out the most impactful parameters that can be optimized to increase permeate production while limiting thermal energy consumption. Finally, the CFD model is used to evaluate the effectiveness of promising designs which have recently been the focus of growing interest: multi-stage AGMD system [32,48] and coupling with solar energy supply [49,50]. The current work focuses on module design and does not consider techno-economic constrains [51], which would arise at later stages of real systems development.

2. Modification of Maxwell-Stefan theory for AGMD

2.1. Setting the stage

In the followings, the authors adopt a 2D cross-sectional representation of an AGMD module as depicted in Fig. 1. According to usual representations [25,31], the module is represented by parallel, adjacent rectangular channels of length L (m): the feed liquid channel (F), isolated by the membrane (M) from the air-gap (AG), bordered by a condensing plate (CP), cooled by contact with the coolant channel (C), with thicknesses noted δ_F (m), δ_M (m), δ_{AG} (m), δ_{CP} (m), and δ_C (m), respectively. The AGMD module representation is associated with a cartesian coordinate system $(O, \vec{x}, \vec{y}, \vec{z})$, centered at the top left corner of the module (feed channel inlet, Fig. 1), where $\vec{x}$ is the unit vector parallel to the membrane surface and pointing in the direction of the gravity vector $\vec{g}$, $\vec{y}$ the unit vector normal to the membrane surface,

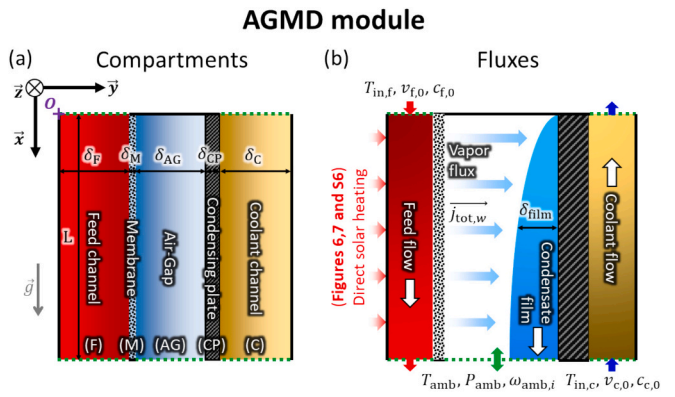


Fig. 1. (a) 2D cross-sectional representation of an air-gap membrane distillation module, in the coordinate system $(O, \vec{x}, \vec{y})$, with (b) a focus on the mass and heat flux within the module and at its boundary. (a) The module length, L (m), feed channel thickness, δ_F (m), cooling plate thickness, δ_{CP} (m), air-gap thickness, δ_{AG} (m), membrane thickness, δ_M (m), and coolant channel thickness, δ_C (m) are indicated. Feed and coolant streams flow along the abscissa axis $(O, \vec{x})$, in parallel with the gravity vector $\vec{g}$. The ordinate axis $(O, \vec{y})$ is normal to the membrane surface. (b) In the AGMD system, the feed and coolant stream flow in counter current direction (white arrow). (b) The vapor flux $\overrightarrow{j_{tot,w}}$ that permeates though the membrane is assumed to condense on the cooling plate surface, forming a film of (horizontal) thickness $\delta_{film}(x)$; then, the liquid condensate flows out of the module under the gravity effect. The plain black lines in (a) and (b) indicate the limits where heat and mass fluxes are assumed to be zero along the direction normal to these module boundary surfaces. Conversely, the dotted green lines in (a) and (b) indicate the boundaries where heat and mass normal fluxes are allowed, representing the inlet/outlet of the systems. In (b) is indicated the module boundary parameters: the inlet feed and coolant temperature $T_{in,f,c}$, inflow velocity $v_{f,c,0}$, inlet salt density $c_{f,c,0}$, and boundary temperature T_{amb}, pressure P_{amb}, and component i mass fraction $\omega_{amb,i}$ at (AG) opening; see details in **§2.2.4**. (b) For scenario detailed in Figs. 6 and 7, a direct solar heating is applied to the feed channel wall, which is effectively represented by an additional inlet diffusive heat flux along (F) wall.

and $\vec{z}$ the unit vector normal to the plan of Fig. 1. In line with common MD model assumptions [52], the variations of physical variables characterizing heat and mass transfer in the AGMD system along $(O, \vec{z})$ are neglected. The temperature $T(x,y)$ (K) and the absolute pressure $p(x,y)$ (Pa) in the module are hereafter described as functions of the x-axis and y-axis position (x,y) in $(O, \vec{x}, \vec{y}, \vec{z})$ only.

Within a general framework for molecular diffusion (not specific to aqueous solution AGMD) [53,54], the gas phase in (M) and (AG) is assumed to be constituted of N compounds i, each characterized by a molar weight M_i (mol kg^{-1}), a molar fraction $x_i(x,y)$, a mass fraction $\omega_i(x,y)$, a partial pressure $p_i(x,y)$ (Pa) and a saturation pressure $p_{sat,i}(T)$ (Pa) associated with a saturation molar fraction $x_{sat,i} = p_{sat,i}/p$. In addition, the air-gap is considered to be open to an isotropic external environment characterized by a pressure p_{amb} (Pa) and a temperature T_{amb} (K), whose default values are those of the ambient environment, 101,350 Pa and 20 °C, respectively. These values are assumed to be the initial pressure and temperature for the gas phase in (M) and (AG), and the values for the external environment.

To demonstrate the capabilities of the theoretical framework, the model is applied to the specific case of extraction of pure water from a seawater feed solution via AGMD under typical conditions [26,30], i.e., with an air-gap at atmospheric pressure and temperature ranges for feed between 20 °C and 80 °C, and a coolant solution at 20 °C. Additionally, the authors consider the use of a seawater type solution as coolant, with the same composition than the feed (cf. **§4**). The physicochemical parameters of seawater solution have been extensively studied over the past decades [55–60]. Notably, the work by Sharqawy et al. [61,62] offers an overview of semi-empirical expressions which give estimations of the mass density ρ_s (kg m^{-3}), the specific heat $C_{p,s}$ (J kg^{-1} K^{-1}), the thermal conductivity k_s (W m^{-1} K^{-1}), and the viscosity μ_s (Pa s), as functions of the pressure, temperature, and salt density. Importantly, these semi-empirical expressions provide accurate approximations with error less than 3 % over a temperature range from 0 °C to at least 100 °C and a salinity range from 0 to at least 150 g/kg [61,62], which are reasonable ranges for the MD device studied in this work. Subsequently, the authors adopt the equations from references [61, 62] to calculate $\rho_{f,c}$, $C_{p,s}$, k_s, and μ_s as functions of $T(x,y)$ and $c(x,y)$ in the feed and coolant channels, and the heat diffusivity coefficient α_s (m^2 s^{-1}) determined as $\alpha_s = k_s/(\rho_s \cdot C_{p,s})$ (see Supplementary Material – SM, section A).

In view of the commonly used module components [45,52], the membrane is assumed to consist of a single layer of hydrophobic porous material (e.g., PVDF [63]) with isotropic structural properties, characterized by a porosity factor ε_M, a pore tortuosity τ_M, and a pore average radius r_M (m). The tortuosity of membrane pores is assumed to be linked to the porosity of the material according to the empirical relation $\tau_M = ((2-\varepsilon_M)/\varepsilon_M)^2$, suitable for membrane distillation representation [64]. In addition, the membrane material is assumed to contain solid spherical inclusions (pellets) that participate in heat conduction along with the gas phase in (M) [65]. In that case, the effective thermal conductivity of the membrane k_M (W m^{-1} K^{-1}) is better represented by a Maxwell Type I equation (for low dense porous material $\varepsilon_M \geq 0.85$ [66]),

$$k_M = k_g \frac{(k_m + 2k_g) + 2(1-\varepsilon_M)(k_m - k_g)}{(k_m + 2k_g) - (1-\varepsilon_M)(k_m - k_g)} \quad (1)$$

where k_m (W m^{-1} K^{-1}) and k_g (W m^{-1} K^{-1}) are the thermal conductivity of the membrane material and of the gas phase inside the membrane (and the air-gap), respectively. The thermal properties of the air-water gas mixture in (M) and (AG) (cf. **§2.2.2**) are estimated using classical kinetic theory for (nonpolar) gases, as functions of the temperature [67]. In a simpler way, the effective heat capacity of the membrane $C_{p,M}$ (J kg^{-1} K^{-1}) is defined by

$$C_{p,M} = \frac{\varepsilon_M \rho_g C_{p,g} + (1-\varepsilon_M)\rho_m C_{p,m}}{\varepsilon_M \rho_g + (1-\varepsilon_M)\rho_m} \quad (2)$$

where $C_{p,g}$ (J kg^{-1} K^{-1}) and $C_{p,m}$ (J kg^{-1} K^{-1}) are the heat capacities; ρ_g (kg m^{-3}) and ρ_m (kg m^{-3}) are the mass densities; ε_M and $(1-\varepsilon_M)$ are the volume fractions of the gas and membrane material, respectively. The expressions (1,2) are used to calculate the effective heat diffusivity coefficient of the membrane α_M (m^2 s^{-1}), defined as $\alpha_M = k_M/(\rho_M \cdot C_{p,M})$, considering the effective mass density ρ_M (kg m^{-3}) given by $\rho_M = \varepsilon_M \rho_g + (1-\varepsilon_M)\rho_m$.

2.2. Modified Maxwell-Stefan formalism for AGMD system

This section presents the equations governing heat and mass transport at each position (x,y) of an AGMD system as depicted in **§2.1**, describing separately the solution flow in (F) and (C) (**§2.2.1**), the gas transport in (M) and (AG) (**§2.2.2**), and the vapor condensation on (CP) (**§2.2.3**). Notably, the authors propose a modified Maxwell-Stefan model for gas transport in (M) and (AG) that accounts for vapor medium saturation. Overall, the authors establish an extensive formalism for the multiphysics of an AGMD module which describes an open system in which the spatial dependence of the physical variables is explicit, and the physical continuity between (F-M-AG-CP-C) and the external environments is ensured by local discrete boundary conditions (**§2.2.4**). Here, the formalism is built with limited use of the usual linear approximations (e.g., equivalent thermal resistance to describe heat transfer [52]) wherever this is not justified by the operating parameters and module dimensions of interest, e.g., for high feed temperatures (cf. **§3**) and meter-long and centimeter-thick modules (cf. **§4**). Eventually, the entire formalism was implemented in a computational fluid

dynamics (CFD) simulation, enabling numerical solutions and predictions of AGMD module performance (**§2.3**).

2.2.1. Feed and coolant flow

Based on MD classical representations [68], the flow regime in the feed and coolant channels in an AGMD module (Fig. 1) is governed by the Navier-Stokes equations. To establish a robust and flexible model with regard to feed and coolant composition and temperature, the liquid phases within the modules are formally considered as weakly compressible fluids characterized by space-dependent physicochemical properties (e.g. density, viscosity), which translates into

$$\begin{cases} \vec{\nabla} \bullet \left(\rho_{\mathrm{f,c}} \vec{v}\right) = -\dfrac{\partial \rho_{\mathrm{f,c}}}{\partial t} \\ \rho_{\mathrm{f,c}} \left(\dfrac{\partial \vec{v}}{\partial t} + (\vec{v} \bullet \vec{\nabla}) \vec{v} \right) = -\vec{\nabla} p + \\ + \vec{\nabla} \bullet \left[\mu_{\mathrm{f,c}} \left(\vec{\nabla} \vec{v} + (\vec{\nabla} \vec{v})^T - \dfrac{2}{3} (\vec{\nabla} \bullet \vec{v}) \mathbf{I} \right) \right] + \rho_{\mathrm{f,c}} \vec{g} \end{cases} \tag{3}$$

where $\vec{v}$ is the liquid-phase velocity field vector (m s^{-1}), p the absolute pressure (Pa), $\rho_{\mathrm{f,c}}$ the density (kg m^{-3}), and $\mu_{\mathrm{f,c}}$ the dynamic viscosity (Pa s) of the solution at position (x,y) in feed and coolant channel, accounting for the gravity acceleration $\vec{g}$ (m s^{-2}). In the notation used above, $\mathbf{I}$ is the identity matrix, $\vec{\nabla}$ and $\vec{\nabla}\bullet$ denotes the gradient and divergence operators, respectively, and $\vec{\nabla}\vec{v}$ is a tensor.

The flow of feed and cooling fluids directly impacts on solution temperature and solute concentration, which in turn affects vapor permeation through the membrane [21,69]. The eq. (3) for fluid motion is then coupled with convection-diffusion equations to describe solute transport in (F) and (C) (Fig. 1):

$$\frac{\partial c_{\mathrm{f,c}}}{\partial t} = \vec{\nabla} \bullet \left(D_{\mathrm{f,c}} \vec{\nabla} c_{\mathrm{f,c}} - \vec{v} c_{\mathrm{f,c}} \right) \tag{4}$$

where $c_{\mathrm{f,c}}$ and $D_{\mathrm{f,c}}$ are, respectively, the solute molar density (mol m^{-3}) and diffusivity coefficient (m^2 s^{-1}) at position (x,y) in (F) and (C). In the same way, the temperature is governed by

$$\frac{\partial T}{\partial t} = \vec{\nabla} \bullet \left(\alpha_{\mathrm{f,c}} \vec{\nabla} T - \vec{v} T \right) \tag{5}$$

where $\alpha_{\mathrm{f,c}}$ (m^2 s^{-1}) are the thermal diffusivity coefficients at position (x,y) in (F) and (C). Eqs. (3–5) describing heat and mass transport are interrelated by expressing energy conservation in (F,C) – the relationship is not reported here, for sake of brevity [45].

Here, the authors consider seawater type solutions in (F) and (C) and so the parameters $\rho_{\mathrm{f,c}}$, $\mu_{\mathrm{f,c}}$ and $\alpha_{\mathrm{f,c}}$ are determined using semiempirical expressions given in SM-A, which describe their (implicit) dependency to the position (x,y) (cf. **§2.1**). Following common assumptions [13,45], the properties of the seawater-type solution are assimilated to those of an aqueous solution with a density of 35 kg m^{-3} of dissolved NaCl. Then, the authors rely on the semi-empirical expression of Wilke and Chang [70] to express the salt diffusion coefficient in the aqueous feed and coolant D_{s} (m^2 s^{-1}), as defined by eq. (S7) (SM-B). In SM section B, the authors argue that other expressions can be used depending on the nature of the solution, and also highlight the temperature dependence of the physicochemical properties for aqueous salt solutions (Fig. S1).

To summarize, eqs. (3–5) combined with eqs. (S1-8) express the interdependence between the velocity field, temperature field, and solute distribution, and provide a rigorous representation of the hydrodynamic behavior of the feed and cooling solution, which is particularly relevant wherever the spatial gradients of the physical variables are exacerbated, e.g., in a large-scale module (cf. **§4**).

2.2.2. Vapor permeate flow in membrane and air-gap

In classical representations of AGMD systems [14], the permeate is produced by vaporization of volatile species from the feed solution in contact with a hydrophobic porous membrane. The gas phase in (M) and (AG) is considered to be composed of a "stagnant" gas, e.g., air, supplied from the external environment (cf. **§2.1**), and volatile compound(s) (e.g. aromatic compounds [43]) originating from the feed solution. In the considered AGMD system (Fig. 1), the temperature difference between the heated feed and cooled air-gap then drive the transport of the gaseous phase through the membrane and the air-gap [21,22]. The diffusive and convective flow of volatile compounds in the (M) and (AG) is also affected by the pressure and composition of the medium [71], as well as the external conditions at the open boundary of the AGMD system with the (ambient) external environment (cf. **§2.2.4**).

The heat transport in the membrane and air-gap is also represented by a convection-diffusion equation, such as T at a given position (x,y) in (M) and (AG) is governed by

$$\frac{\partial T}{\partial t} = \vec{\nabla} \bullet \left(\alpha_{\mathrm{M,g}} \vec{\nabla} T - \vec{u} T \right) \tag{6}$$

where $\alpha_{\mathrm{M,g}}$ (m^2 s^{-1}) is the heat diffusivity coefficient of either the membrane, using eqs. (1,2), or the air-water gas mixture in (AG) [67], and $\vec{u}$ (m s^{-1}) is the velocity field for the gas phase, which is assumed to be continuous between (M) and (AG). Similarly, $\vec{u}$ is described differently between the air-gap, which is governed by a Navier-Stokes equation for compressible fluid (cf. eq. (3)), and within the membrane, where the gas flow is necessarily constrained by the medium porosity ε_{M}, and the flow velocity is better represented by the Brinkmann equation [13]

$$\begin{cases} \dfrac{\partial (\varepsilon_{\mathrm{M}} \rho_{\mathrm{g}})}{\partial t} + \vec{\nabla} \bullet \left(\rho_{\mathrm{g}} \vec{u} \right) = 0 \\ \dfrac{\rho_{\mathrm{g}}}{\varepsilon_{\mathrm{M}}} \left(\dfrac{\partial \vec{u}}{\partial t} + (\vec{u} \bullet \vec{\nabla}) \dfrac{\vec{u}}{\varepsilon_{\mathrm{M}}} \right) = -\vec{\nabla} p + \vec{\nabla} \bullet \left[\dfrac{\mu_{\mathrm{g}}}{\varepsilon_{\mathrm{M}}} \left(\vec{\nabla} \vec{u} + (\vec{\nabla} \vec{u})^T - \dfrac{2}{3} (\vec{\nabla} \bullet \vec{u}) \mathbf{I} \right) \right] - \left(\kappa^{-1} \mu_{\mathrm{g}} \right) \vec{u} + \rho_{\mathrm{g}} \vec{g} \end{cases} \tag{7}$$

where μ_{g} (Pa s) is the gas mixture viscosity [72]. In eq. (7), κ (m^2) is the membrane permeability to convective flux that could be estimated using the Ergun expression $\kappa = (2r_{\mathrm{M}})^2 \varepsilon_{\mathrm{M}}^3 / \left[150 (1-\varepsilon_{\mathrm{M}})^2 \right]$ for non-Darcian flow and assimilating the membrane to a packed-bed of pellets [73]. Please note that the equation for fluid motion in the air-gap can be formally derived from eq. (7) by taking $\varepsilon_{\mathrm{M}} = 1$.

According to common representations [27], the gaseous phase inside (M) and (AG) is first assumed to act as an ideal gas mixture which tends to equilibrate with the external environment (Fig. 1), without considering additional constraints that could generate forced convection of the vapor, e.g., gas injection in the case of sweeping gas membrane distillation [74]. For the sake of generality, each molecular component i is considered to be subjected to a mass convective flux $\overrightarrow{j_{\mathrm{c},i}}$ (kg m^{-2} s^{-1}) expressed as [53]

$$\overrightarrow{j_{\mathrm{c},i}} = \rho_{\mathrm{g}} \omega_i \vec{u} \tag{8}$$

where $\rho_g\omega_i$ (kg m^{-3}) correspond to the mass density of component i, and $\vec{u}$ (m s^{-1}) is governed by eq. (7). Thus, $\vec{j_{c,i}}$ contribution to the total flux could be negligible in the air-gap, e.g., under isobaric conditions. Within the membrane, vaporization of volatile compounds at the feed/membrane interface (cf. **§2.2.4**) induces a pressure gradient which, in turn, generates locally a convective flow (cf. **§3** and **§4**).

To represent the diffusive mass transport in (M) and (AG), the authors employ the so-called Maxwell-Stefan model [75] that describes the multi-diffusion of gaseous (or liquid) mixtures of molecules, which are assumed to be non-interacting, i.e., assuming no state change or chemical transformation of compounds [76]. In the gaseous phase confined between the feed/membrane interface (F/M) and the condensate film surface (Fig. 1b), the mass diffusive flux $\vec{j_{d,i}}$ (kg m^{-2} s^{-1}) of a volatile compound i among a gas mixture with N compounds, is first expressed through the generalized Fick equation [53,54,71,77]

$$\vec{j_{d,i}} = -\rho_g\omega_i\sum_{k=1}^{N}\left(\widehat{D}_{k,i}\vec{d_k}\right) - D_i^T\frac{\vec{\nabla}T}{T} \tag{9}$$

where the index k holds for any compounds of the mixture (including i), $\widehat{D}_{k,i}$ (m^2 s^{-1}) is the Fick multicomponent diffusion coefficient for a gas pair (k,i) or Fick self-diffusion coefficient for $k = i$, and D_i^T (kg m^{-1} s^{-1}) is the so-called thermodiffusion coefficient [78] of species i at temperature T, which can be estimated using the semi-empirical formula provided by Bartlett et al. [79]. In eq. (9), $\vec{d_k}$ (m^{-1}) denotes the driving force for the diffusion of a component k, and its expression is derived from considerations about the free Gibbs energy of the gas mixture [80]

$$\bar{c}_g RT\vec{d_i} = x_i\bar{c}_g\left(\sum_{k=1}^{N-1}\left(\frac{\partial\bar{G}_i}{\partial x_k}\right)_{T,p}\vec{\nabla}x_k\right) + (x_i-\omega_i)\vec{\nabla}p - \omega_i\rho_g\vec{g_i} + \omega_i\sum_{k=1}^{N}\omega_k\rho_g\vec{g_k} \tag{10}$$

where $\bar{c}_g$ (mol m^{-3}), and ρ_g (kg m^{-3}) are, respectively, the molar and mass concentration of the gas mixture, and $\bar{G}_i$ (J mol^{-1}) the partial molar Gibbs free energy, i.e., the chemical potential of species i. The species of index N is conveniently assigned to the solvent. The expression (10) encompasses three physical contributions that drive diffusion (from left to right): the composition gradient; the pression gradient; and the external forces effect, represented by the force vector $\vec{g_i}$. It is important to recall that, according to eqs. (9,10) (cf. work by Curtiss et al. [54]), the diffusion flows of each component are interdependent, such as $\sum_{k=1}^{N}\vec{d_k} = 0$, $\sum_{k=1}^{N}\omega_k\widehat{D}_{k,i} = 0$ and $\sum_{k=1}^{N}D_k^T = 0$.

As discussed by Ekström [81], $\vec{g_i}$ (m s^{-2}) represents the friction exerted by the pore wall on the molecules i while diffusing in the porous membrane (cf. **§2.1**), following the classical framework of Knudsen diffusion [82], which is translated into the expression

$$\vec{g_i} = -\frac{\bar{c}_g x_i RT}{\rho_g\omega_i D_i^K}\left(\frac{\vec{j_{d,i}}}{\rho_g\omega_i} + \vec{u_W}\right) \tag{11}$$

where D_i^K (m^2 s^{-1}) is the Knudsen diffusion of molecule i in the membrane, expressed as

$$D_i^K = \frac{8}{3}r_M\sqrt{\frac{RT}{2\pi M_i}} \tag{12}$$

with R the gas constant. In eq. (11), $\vec{u_W}$ (m s^{-1}) represents the flow velocity in the near-surface region of the pore wall, where most of the gas molecules colliding with the pore wall are assumed to reside [81,83]. By assuming, additionally, a no-slip condition at the pore-wall surface, $\vec{u_W}$ can be determined using eqs. (9,10) for $\vec{d_i} = 0$ [81].

In eq. (10), the driving force relative to the medium composition is related to the molar fraction gradient $\vec{\nabla}x_i$ and the partial derivative of $\bar{G}_i$, the chemical potential of species i, with respect to the molar fraction at constant temperature and pressure. In the literature on gas transport representations [53,54], it is used the relation $d\bar{G}_i = RT(d\ln(a_i))$ where a_i is the activity coefficient of species i and is most of the time replaced by the molar fraction x_i, according to the ideal gas mixture assumption which holds for low solute concentrations. However, following the common assumption [53,54], the expression of the flux resulting from the (numerical) resolution of eqs. (7,8) will not account for physical limitation on the value of x_i, such as medium saturation [47]. These considerations, together with preliminary simulations, have led us to modify the Maxwell-Stefan model to account for medium saturation, in the particular case of water/air diffusion.

In standard conditions, namely, (M) and (AG) at atmospheric pressure and 20 °C $\leq T \leq$ 80 °C (cf. **§2.1**), the saturated vapor pressure of water is lower than the absolute pressure, which implies that the molar fraction of water vapor shall be inferior to $x_{sat,w} = p_{sat,w}/p$ at a given position (x,y). The subscripts w and a hereafter indicate variables that characterise water vapor and air, respectively. The water condensation is assumed to occur mainly at the surface of (CP) (Fig. 1), and also that the phase inside the membrane pore and the air-gap, excluding the condensate film, is composed solely of a binary gas mixture of water and air, which, for the sake of simplicity, is considered as an ideal gas. Hence, it results that the total water fraction x_w in this gaseous phase is lower than $x_{sat,w}$. To account for this constraint in eqs. (9,10), the authors then reconsider the organizational molar entropy $\bar{S}$ (J K^{-1} mol^{-1}) of the gas mixture, inspired from the works of Brown [84], as a function of water vapor and air molar fraction, x_w and x_a respectively,

$$\bar{S} = -R(1-x_{sat,w})(x_w\ln(x_w) + x_a\ln(x_a)). \tag{13}$$

Eq. (13) represents the molecular distribution corresponding to an entropy maximum for the gaseous medium in (M) and (AG) at equilibrium, which is partially saturated with water vapor. The prefactor $(1-x_{sat,w})$ therefore represents the change in entropy resulting from the reduction in sites available for the distribution of water and air molecules in the medium, due to the saturated vapor limit. Consequently, for the expression of the diffusion driving force (Eq. (10)), the relation $\left(\partial\bar{G}_{w,a}/\partial x_{w,a}\right)_{T,p} = -RT(1-x_{sat,w})/x_{w,a}$ is obtained with respect to chemical potentials depending on $\bar{S}$.

The above eqs. (6–13) combined with the expressions (1,2), enable to determine $\vec{j_{tot,w,a}} = \vec{j_{c,w,a}} + \vec{j_{d,w,a}}$ (kg m^{-2} s^{-1}), which is the total mass flux for water vapor and air in (M) and (AG), and can also be straightforwardly transposed to other gas mixture compositions (with or without saturation constrain). Finally, by analytically solving the system of eqs. (9,10) and substituting the parameters by the expressions (11,13), the diffusive flux of water and air for the gas phase in the membrane are expressed as:

$$\begin{cases} \vec{j_{d,w}} = \left(\dfrac{\omega_a x_w}{D_w^K\omega_w} + \dfrac{\omega_w x_a}{D_a^K\omega_a} + \dfrac{1}{\widehat{D}_{a,w}}\right)^{-1}\left[\rho_g\left(\dfrac{\omega_a x_w}{D_w^K} - \dfrac{\omega_w x_a}{D_a^K}\right)\vec{u_W} - \rho_g\left((1-x_{sat,w})\vec{\nabla}x_w + (x_w-\omega_w)\dfrac{\vec{\nabla}p}{p}\right) - \dfrac{D_w^T}{\widehat{D}_{a,w}}\dfrac{\vec{\nabla}T}{T}\right] \\ \vec{j_{d,a}} = \left(\dfrac{\omega_a x_w}{D_w^K\omega_w} + \dfrac{\omega_w x_a}{D_a^K\omega_a} + \dfrac{1}{\widehat{D}_{a,w}}\right)^{-1}\left[\rho_g\left(\dfrac{\omega_w x_a}{D_a^K} - \dfrac{\omega_a x_w}{D_w^K}\right)\vec{u_W} - \rho_g\left((1-x_{sat,w})\vec{\nabla}x_a + (x_a-\omega_a)\dfrac{\vec{\nabla}p}{p}\right) - \dfrac{D_a^T}{\widehat{D}_{a,w}}\dfrac{\vec{\nabla}T}{T}\right] \end{cases} \tag{14}$$

The system of eqs. (14) for the water and air diffusive fluxes with account of the vapor medium saturation, is a major result of this work. The saturation correction factor (eqs. (14)) effectively limits the non-physical situation in which the water molecular diffusion could, at a given location (x,y) in the membrane or air-gap, generate a partial pressure of water greater than the saturated vapor pressure at the local temperature, assuming that water condensation occurs mainly at the condensing plate surface. Note that most AGMD models in the literature are currently based on analytical solutions of the Maxwell-Stefan model, which disregards this physical consideration arising from the discretization of the medium, by directly estimating the vapor flux from the temperature and vapor pressure boundary values at the Feed/Membrane and Air-Gap/Condensing plate interfaces [27–32].

In the air-gap, the Knudsen diffusion contribution is neglected, i.e., $\overrightarrow{j_{\mathrm{d},w,a}}$ in (AG) is simply obtained by removing all the terms containing $D^{K}_{w,a}$ in eq. (14). From reference [54], the Fick diffusion coefficient in eq. (14) is related to $D_{w,a}$ ($\mathrm{m^2\ s^{-1}}$) the Maxwell diffusion coefficient for a binary mixture (w,a), such as $\widehat{D}_{w,a} = -\frac{\omega_a}{\omega_w}\widehat{D}_{a,a} = -\frac{\omega_w}{\omega_a}\widehat{D}_{w,w} = \frac{\omega_a\omega_w}{x_a x_w}D_{w,a}$, with the additional relation $\widehat{D}_{a,w} = \widehat{D}_{w,a}$. For a water/air mixture, the Maxwell diffusion coefficient is estimated using the semi-empirical expression:

$$D_{w,a} = \frac{\left(p_{\mathrm{c},w}p_{\mathrm{c},a}\right)^{\frac{1}{3}}\cdot\left(T_{\mathrm{c},w}T_{\mathrm{c},a}\right)^{\frac{5}{12}}\cdot\left(M_w^{-1}+M_a^{-1}\right)\cdot\left(3.640\cdot10^{-8}\right)}{p} \cdot\left(\frac{T}{\sqrt{T_{\mathrm{c},w}T_{\mathrm{c},a}}}\right)^{2.334} \tag{15}$$

as a function of p (atm) and T (K) at a position (x,y) in (M) and (AG), and where $p_{\mathrm{c},w}$ (atm) and $p_{\mathrm{c},a}$ (atm), $T_{\mathrm{c},w}$ (K) and $T_{\mathrm{c},a}$ (K) are the critical pressures and temperatures of water and air, respectively [53].

The formalism developed in this section gives access to the temperature, as well as the water and air fluxes in any position (x,y) in the membrane and air-gap (excluding the condensate film). As mentioned previously, eqs. (9,10,14) highlight the fact that water vapor in the membrane and air-gap diffuses against the diffusive flow of air, within the binary water/air mixture.

2.2.3. Film condensation in AGMD

In the considered AGMD module (Fig. 1), permeate recovery is part of the distillation process and is driven by the temperature difference between the feed channel and the cooled condensing plate (CP). Subsequently, the (CP) surface is assumed to be the area where the permeate would condensate, neglecting aerosol formation or lateral wall contribution. Additionally, no specific hydrophobic surface property is considered for the (CP) that could promote the formation of droplets that sweep away from the condensing plate surface, i.e., dropwise condensation [85]. In return, the permeate is assumed to condense into a liquid film on the surface of (CP), which flows out of the opening of (AG) under the effect of gravity [86,87]. Inspired from the works by Brouwers [88,89], it is also assumed that the thin film is formed by condensation of the steam flow normal to the (CP) surface, and that the film flow is laminar and governed by the Navier-Stokes equations. Neglecting the film growth acceleration along the direction normal to the gravity vector $(O,\vec{y})$, the film thickness δ_{film} (m) at a given position x along the (CP) surface (Fig. 1b) can be approximated, for the case of water condensation, by

$$\delta_{\mathrm{film}}(x) \approx \left(\frac{3\mu_{\mathrm{film}}\int_0^x\left(\overrightarrow{j_{\mathrm{tot},w}}\bullet\vec{y}\right)dx}{\rho^2_{\mathrm{film}}(\vec{g}\bullet\vec{x})}\right)^{\frac{1}{3}} \tag{16}$$

where μ_{film} (Pa s) and ρ_{film} ($\mathrm{kg\ m^{-3}}$) are the film viscosity and density, respectively. The integral term of eq. (16) highlights that film thickness at a given vertical position x depends on the cumulative flux of condensed steam above it (from 0 to x). One can argue that, although condensation would initially take place via droplet formation on the surface of the condensing plate, a full-scale module and/or a high vapor flow would lead to a consequent water droplet sweeping which, *in fine*, could be formally assimilated to a filmwise condensation phenomenon under steady state conditions [90]. For the sake of completeness, the heat transfer within the film is described by a convection-diffusion equation accounting for fluid flow velocity, film thickness and thermal properties of the liquid condensate (cf. eq. (5)).

2.2.4. Boundary conditions for the AGMD module

This sub-section describes the AGMD module boundary conditions with the exterior environment and between the physical domains defined in **§2.2.1**, **§2.2.2** and **§2.2.3**, inspired from common model assumptions [45]. The heating and cooling system for feed and coolant solutions are regarded as external processes to the system, which are effectively represented by inlet temperatures $T_{\mathrm{in,f}}$ (K) and $T_{\mathrm{in,c}}$ (K) (Fig. 1a). At the outlet of channels (F) and (C), it is simply assumed that the temperature gradient in the normal direction of the outlet is zero (constant flux). Conversely, at the opening (AG), the authors consider *a priori* that there can be a heat exchange with the external environment (cf. **§2.1**), which is represented by a Danckwerts boundary conditions (neglecting thermal expansion) [91],

$$\begin{cases} k_g\left.\dfrac{\partial T}{\partial x}\right|_{x=L^-} = \rho_g\left(\displaystyle\int_{T_{\mathrm{amb}}}^{T(L,y)} C_{\mathrm{p,g}}dT\right)\vec{u}\bullet\vec{x}, & \text{if } \vec{u}\bullet\vec{x}<0 \\ k_g\left.\dfrac{\partial T}{\partial x}\right|_{x=L^-} = 0, & \text{else} \end{cases} \tag{17}$$

where the left-hand term corresponds to the conductive heat flow in (AG). In relation (17), the right-hand term models the heat inflow from the external (ambient) environment in the case of an inflow ($\vec{u}\bullet\vec{x}<0$ at (AG) opening), else, the temperature variation is considered zero at (AG) opening. For other external boundaries, the AGMD module walls are assumed to be thermally insulating, effectively assuming that the temperatures on either side of this physical boundary are equal, e.g., along left feed channel wall $T(x,0^-) = T(x,0^+)$ (Fig. 1).

Inside the AGMD module, the water vaporization at the feed/membrane interface, brings additional latent energy, such as

$$k_{\mathrm{f}}\left.\frac{\partial T}{\partial y}\right|_{y=\delta_{\mathrm{F}}^-} - \rho_{\mathrm{f}}C_{\mathrm{p,f}}T(\vec{v}\bullet\vec{y}) = k_g\left.\frac{\partial T}{\partial y}\right|_{y=\delta_{\mathrm{F}}^+} + \left(\overrightarrow{j_{\mathrm{tot},w}}\bullet\vec{y}\right)\Delta H_{\mathrm{vap,s}} \tag{18}$$

where k_{f} ($\mathrm{W\ m^{-1}\ K^{-1}}$) and k_g ($\mathrm{W\ m^{-1}\ K^{-1}}$) are the thermal conductivities of the feed solution and gas phase in the membrane, respectively (cf. **§2.1**). In relation (18), $C_{\mathrm{p,f}}$ ($\mathrm{J\ kg^{-1}\ K^{-1}}$) is the feed specific heat capacity given by eq. (S2) (SM-A), and $\Delta H_{\mathrm{vap,s}}$ ($\mathrm{J\ kg^{-1}}$) is the latent heat of evaporation of a seawater type solution given by eq. (S5) (SM-A), both defined as functions of the temperature and salt concentration at the (F/M) interface. In eq. (18), the left and right-hand terms correspond to the heat flux at F/M interface, on the feed and membrane side respectively. Conversely, at the condensate film surface in the (AG), there is a negative contribution to the heat flux of the latent heat of condensation, such as

$$k_g\left.\frac{\partial T}{\partial y}\right|_{y=y_{\mathrm{film}}^-} + \left(\overrightarrow{j_{\mathrm{tot},w}}\bullet\vec{y}\right)\Delta H_{\mathrm{vap}} = k_{\mathrm{film}}\left.\frac{\partial T}{\partial y}\right|_{y=y_{\mathrm{film}}^+} \tag{19}$$

with k_{film} ($\mathrm{W\ m^{-1}\ K^{-1}}$) being the film thermal conductivity and y_{film} (m) the film surface position along $(0,\vec{y})$, defined by $y_{\mathrm{film}} = \delta_{\mathrm{F}} + \delta_{\mathrm{M}} + \delta_{\mathrm{AG}} - \delta_{\mathrm{film}}(x)$ assuming that $\delta_{\mathrm{AG}} \gg \delta_{\mathrm{film}}(x)$ (cf. **§3 and §4**, and e.g. ref. [26]). To ease the computation, the authors estimate in eq. (19) that $y_{\mathrm{film}} \approx \delta_{\mathrm{F}} + \delta_{\mathrm{M}} + \delta_{\mathrm{AG}}$. In eq. (19), the latent heat of condensation ΔH_{vap} ($\mathrm{J\ kg^{-1}}$) is formally obtained by eq. (S5) for a zero-salt concentration, assuming pure water condensation. Lastly, heat transport at the interfaces between the condensate film and the (CP), and between (CP) and the coolant, is transferred by conduction. The heat transport

through (CP) is also considered to be purely conductive. As a side note, the recovery process of the vapor could be externalized to the AGMD process by a condenser [43], which would erase the condensate contribution to the cooling of the air-gap.

For the external boundary conditions related to mass transport, a no-slip condition is considered along the module wall (Fig. 1). At the feed and coolant inlet, the velocity field is considered to have a classical parabolic profile with an average value $v_{f,0}$ (m s^{-1}) and $v_{c,0}$ (m s^{-1}), respectively. At the feed and coolant outlet, the outflow is conserved. At the (AG) opening, the authors consider *a priori* the possibility of having either a conserved outflow or an inflow of moist air (cf. eq. (17)).

Inside the AGMD module, at the (F/M) interface and at the surface of the condensation film, the water partial pressure is considered to be equal to the saturation vapor pressure (evaporation and condensation), using the expression of the vapor saturation pressure $p_{sat,w,s}$ given by eq. (S6) to account for the salt concentration at the (F/M) interface (SM-A). A pressure equilibrium is assumed between the gas and liquid phases at the (F/M) interface, and between the inner and external environment at the (AG) opening. In addition to the previous boundary conditions, it is necessary to consider a sufficient quantity of air outside the system, e.g., $\omega_{amb,a} \geq 0.1$, to be able to compute the convective and diffusive flows of air and water vapor in the air-gap, else the (AG) will tend to be fully saturated in water (cf. eqs. (10,14)).

As additional issue, water permeation leads to non-volatile compounds accumulation at the (F/M) interface, which has an impact on solution hydrodynamics, solute retention, and membrane permeate flux [35,36]. MD models most often adopt the *gel layer theory* to describe this so-called concentration polarization effect [30], notably based on the historical works by Porter [92]. Rather than including the analytical expression estimating the concentration of salt retained at the interface, the authors simply apply the initial hypothesis of Porter theoretical developments [92],

$$\left(\frac{\overrightarrow{j_{tot,w}}\left(x,\delta_F^+\right)}{\rho_f\left(x,\delta_F^-\right)} \bullet \vec{y}\right) c_f\left(x,\delta_F^-\right) = D_f\left(x,\delta_F^-\right)\left.\frac{\partial c_f}{\partial y}\right|_{y=\delta_F^-} \tag{20}$$

where $\overrightarrow{j_{tot,w}}\left(x,\delta_F^+\right)$ (kg m^{-2} s^{-1}) is the water vapor flux on the membrane side, $c_f\left(x,\delta_F^-\right)$ and $\left.\partial c_f/\partial y\right|_{y=\delta_F^-}$ are, respectively, the retained salt concentration and the concentration gradient feed side at position x along the (F/M) interface (Fig. 1). In Porter theory [92], assuming pure solvent permeation, the normal flow resistance of the *gel layer*, that is, the dynamic (dense) layer of solute accumulated at the membrane surface, will adjust so that the convective transport by the solvent of species retained to the membrane (left-hand side eq. (20)) is equal to the back-diffusive transport of salt (right-hand side eq. (20)). In a consistent way, water evaporation generates a feed flow normal to the (F/M) interface, whose velocity is then (considering momentum conservation),

$$\vec{v}\left(x,\delta_F^-\right) = \frac{\overrightarrow{j_{tot,w}}\left(x,\delta_F^+\right)}{\rho_f\left(x,\delta_F^-\right)}. \tag{21}$$

In combination with eqs. (1–8,14) and (S1-6), the boundary relations (20,21) allow to represent rigorously the hydrodynamic effects of solvent (water) evaporation accompanied with solute (salt) retention at the vicinity of the membrane surface.

2.3. Numerical solution of the modified Maxwell Stefan model for AGMD

The complete formalism developed in **§2.2** and SM-A was implemented and solved numerically by means of an algorithm developed within COMSOL Multiphysics 6.2 ® software, prescribing an exhaustive list of parameters characterizing the external environment properties (inlet/outlet values), module components dimensions, membrane material properties (porosity, thermal conductivity, density, heat capacity, etc.), as well as, feed, coolant, and gas phase physicochemical properties, initial composition and state (initial temperature and velocity fields, solute distribution, etc.). A key feature of this model is the explicit discretization of the membrane domain. While most studies simplify the membrane by applying boundary conditions at its surfaces [27–32], here the membrane is treated as a distinct computational domain, as for all module components. This approach enables a more accurate description of internal transport phenomena at the cost of increased computational demand. Moreover, the formalism was solved under steady state conditions in order to represent the operation of an AGMD system in a continuous regime, such as for the experiments conducted in this work (**§3**) and for full-scale installations [33,93].

One of the main difficulties in solving our complete AGMD process formalism lies in the spatial discretization of the module. Consequently, a triangular mesh was implemented to allows smooth calculation of the variables' bulk values, combined with a fine square mesh at the (F/M), (M/AG), and (AG/CP) interfaces to accurately capture the heat and mass gradient that are key to providing physically reliable values about, e.g., permeate flux and condensate film formation. To optimize the computation without compromising model accuracy, the mesh scale is increased by a factor of 4 to 8 in the direction of the module length, resulting in a simulation time of the order of 15 min to 1 h on a recent computer set-up.

3. Experimental validation

To assess the CFD model validity, experimental measurements were conducted on pure water and seawater-type solution distillation, using a laboratory-scale AGMD set-up. The experimental device was custom-built using a commercial MD module and following the standards set out in the literature, in order to provide reference data from a controlled AGMD module configuration. A photograph and a diagram of the experimental setup are presented in the supplementary materials, Fig. S2. The key parameters related to the module's dimensions and characteristics, as well as its operating conditions, are specified in Table 1. The lower part of the air gap membrane module is open throughout its thickness and width to allow liquid condensate to flow freely out of the (AG), thus preventing flooding, to be collected outside (Fig. S2). The experiments consisted of measuring permeate mass production every 10

Table 1
AGMD module characteristics of the lab-scale setup and used for model validation through CFD simulations.

Parameters	Values	Descriptions
$T_{in,c}$	293.15 K	Coolant inlet temperature
$T_{in,f}$	[30.8 °C, 40.7 °C, 51.6 °C, 61.4 °C, 70.5 °C, 80.6 °C]	Bulk feed inlet temperature – iterative variable
$v_{c,0}$	0.58295 m s^{-1}	Average inlet coolant velocity
$v_{f,0}$	0.060822 m s^{-1}	Average inlet feed velocity
$c_{f,0}$	35 kg m^{-3}	Inlet feed salt concentration
W	0.0953 m	Module width along $(O, \vec{z})$
L	0.146 m	Channel length along $(O, \vec{x})$
$\delta_{F,C}$	0.003 m	Feed and coolant channel thickness
δ_{AG}	0.005 m	Air-gap thickness
δ_M	1×10^{-4} m	Membrane thickness
δ_{CP}	0.0019 m	Condensing plate thickness
k_{CP}	152 W m^{-1} K^{-1}	Condensing plate thermal conductivity
k_m	0.25 W m^{-1} K^{-1}	Membrane material thermal conductivity
ρ_m	2,200 kg m^{-3}	Membrane material density
$C_{p,m}$	1,050 J kg^{-1} K^{-1}	Membrane material heat capacity
r_M	2.2×10^{-7} m	Pore radius
ε_M	0.85	Membrane porosity
τ_M	1.8304	Pore tortuosity
T_{amb}	293.15 K	Ambient temperature
p_{amb}	101,330 Pa	Ambient pressure
$\omega_{amb,w}$	0.022913	External water vapor fraction

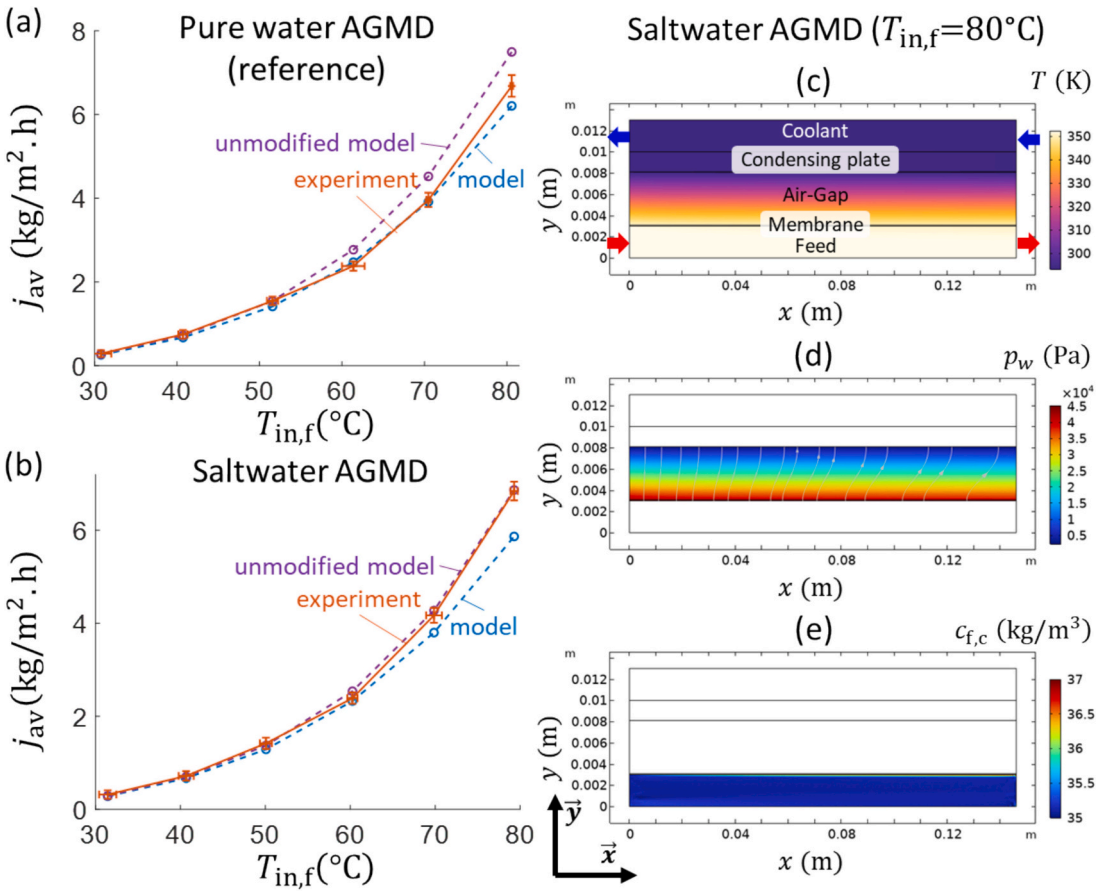


Fig. 2. Average permeate steady-state flux j_{av} for (a) pure water and (b) salt water distillation (NaCl 35 kg m^{-3}). The crosses linked by a solid line (orange) represent the average experimental value for a given feed temperature, with the one standard deviation relative to the feed temperature and the permeate flow measurements. The circles represent the predictions from the modified Maxwell-Stefan diffusion model (blue) modified and (purple) unmodified for medium vapor saturation (cf. Eqs.(13,14), main text **§2.2**), with the input parameters given in Table 1. Simulated lab-scale AGMD flat-sheet module (c) temperature $T(x,y)$, (d) water partial pressure $p_w(x,y)$ in (M) and (AG), (e) salt distribution $c_{f,c}(x,y)$ in (F) and (C), for the parameter given in Table 1, and for feed and coolant inlet temperatures of $T_{in,f}$ = 80 °C and $T_{in,c}$ = 20 °C, respectively. (c,d,e) The vertical orientation of the module is indicated by the vector $\vec{x}$.

min over an 80-min period (8 replicas) at each fixed bulk feed inlet temperature in order to obtain the steady permeate flux averaged over the membrane active surface, and gradually increasing the feed temperature from 30 °C to 80 °C, with 10 °C steps. At the beginning of each experiments, the feed and cooling flow rates were set at 63 L/h and 600 L/h, respectively, in counter current flow configuration, with a coolant consisting of a 20 % glycol-water solution whose temperature was kept constant at 20 °C using an external cryostat (Fig. S2). The first series of reference measurements was carried out using pure water as liquid feed, to verify the proper functioning of the AGMD module (Fig. 2a). For the second series of measurements (Fig. 2b), the module distilled an aqueous solution with a NaCl concentration of 35 kg m^{-3}, which was kept constant during the experiment by monitoring the conductivity and replenishing pure water to re-dilute the feed solution. A commercial PVDF membrane produced by GVS Filter Technology® was employed.

The authors intentionally used an oversized cooling system to ensure that the uncertainty in the inlet coolant temperature was negligible in comparison to that in the feed. The sources of uncertainty with the greatest impact on the results were identified as coming directly from the measurement of the permeate flux at a given feed inlet temperature and from the control of the same temperature. Fig. S2c provides estimation on measured quantity uncertainties from the installation components: cooler, feed pump and heating system, scale. Figs. 2a and b indicates the average flux values (crossed points). For each data point, the standard deviation relative to the measured flux values (vertical bar), and the standard deviation from the mean temperature of the measured feed inlet temperature values (horizontal bar) are reported.

Fig. 2 compares the experimental results and the model predictions of the values of membrane-surface averaged permeate mass flux, j_{av} (kg m^{-2} s^{-1}) at steady-state, for both pure water (Fig. 2a) and salt water (Fig. 2b) distillation, as a function of the feed inlet temperature $T_{in,f}$ (K). As expected, Fig. 2 shows that j_{av} increased with $T_{in,f}$ in both the experiment and model predictions, for all other parameter kept constant. Comparing experimental results from Fig. 2a and Fig. 2b, j_{av} was slightly higher for saltwater feed and at high temperature ($T_{in,f} \geq 70$ °C). Moreover, for saltwater distillation (Fig. 2b), conductivity measurements in the recovered liquid permeate indicate salt rejection values that changed from above ~99.9 % for $T_{in,f} \leq 70$ °C to ~98 % for $T_{in,f}$ = 80 °C. Figs. 2a and b overlay the results of the CFD model with the input parameters defined in Table 1, with (blue curves) and without (purple curves) the modification of the Maxwell-Stefan model for medium vapor saturation (Eq. (14)). In addition, Figs. 2c-e shows the temperature $T(x,y)$ within the module, the water vapor pressure $p_w(x,y)$ in (AG), and the salt distribution $c_f(x,y)$ in (F), under steady-state conditions and for an inlet feed temperature of 80 °C, accounting for (M-AG) vapor saturation. In the lab-scale configuration, $T(x,y)$ decreased from the feed to the coolant with negligible temperature variation following the feed and coolant streams (Fig. 2c). Accordingly, the water vapor pressure was higher towards the membrane region, and the vapor flowed into the air-gap to condense on the cooled condensing plate (grey arrow, Fig. 2d). As

water evaporation at (F/M) interface is accompanied by salt retention on the feed side, a dense "layer" of salt is formed in the vicinity of the membrane surface (thin yellow-red band) that was predicted to become denser along the feed stream (Fig. 2e). Figs. 2a and b shows that the model accurately fitted the experimental values of j_{av}, for 30 °C ≤ $T_{in,f}$ ≤ 50 °C: the prediction were within the error bars. Indeed, as mentioned in **§2.2.2**, saturation correction had negligible impact on the vapor flux under low temperature conditions, at which the density of water vapor generated at the interface (F/M) is relatively low. Conversely, at higher temperatures, for $T_{in,f}$ ≥ 50 °C, the evaporation rate of water from the feed is higher and ignoring vapor saturation in (M-AG) led to an overestimation of j_{av}, while the modified model predictions accurately fitted the experimental results for pure water distillation (Fig. 2a). For saltwater AGMD and for $T_{in,f}$ > 60 °C, the modified CFD model underestimated permeate flux for higher temperatures (Fig. 2b). The model assumed only vapor permeation and complete salt retention at (F/M) interface (Eq. (20)). However, experimental measurements indicated a deviation from this "ideal" behavior of the module physics, with the presence of salt in the condensate. The permeation of non-volatile salt through the membrane can have various origins, including but not limited to membrane *wetting* [93]. Hence, as the CFD model did not account for this unpredictable flux, the j_{av} predictions were lower than the experimental result in the case of Fig. 2b.

In addition to our own validation experiments, the model performance was tested on AGMD experimental results available in the literature, in particular those of Choi et al. [32], and although the authors did not have access to all the information relating to their work, the predictions obtained with the model were of the same order of magnitude to their experimental values and the predictions of their own CFD model (Fig. S3). For the sake of completeness, the predictions of the unmodified model are also shown, and Fig. S3 indicates that not accounting for medium vapor saturation yielded an overestimation of the permeate flux for increasing feed inlet temperatures. Other less complete datasets found in the literature were also used to validate the model development (*data not shown*).

As an intermediate conclusion, comparison with experimental results confirms the ability of our CFD model to accurately predict the operation of the AGMD for (sea)water distillation at low to medium feed temperatures (30 °C ≤ $T_{in,f}$ ≤ 50 °C). Furthermore, comparison with a real AGMD system highlighted the limitations of the current model in handling non-ideal behaviors of the module due to unpredictable phenomena that are complex to formalize (e.g., wetting, fouling) and favored by higher permeate flux conditions (e.g., high feed-coolant temperature difference) [31,94]. The following simulations were then all performed based on the tested experimental setup and for operating conditions where the validity of the model was assumed to hold, i.e. for $T_{in,f}$ ≤ 60 °C.

4. Model exploration of AGMD system designs and performance

In this section, the model presented in *§2* is used to explore the optimal design of AGMD modules within different configurations, notably by predicting their efficiency in terms of permeate production and thermal power consumption. The authors proposed scenario where plate-and-frame module dimensions and operating conditions varied (Fig. 3a), namely, feed/coolant channel length and thickness, airgap thickness, feed inlet temperature, and inlet flow velocity, to highlight how these important parameters influence the performance of a full-scale AGMD module for desalination (*§4.1*). The next scenario proposes a system consisting of three large AGMD modules connected in series (Fig. 3b) and evaluate the overall permeate production rate and the benefit of such an installation (**§4.2**). Finally, the authors consider the addition of direct solar irradiation for heating the feed solution within the module (Fig. 3c), under low-temperature operating conditions (**§4.3**). Within the theoretical framework, the direct solar heating applied to the feed channel wall was effectively represented by an additional inlet diffusive heat flux along the feed channel wall. In the simulations, it is assumed that saltwater can be used for cooling, that is, the AGMD system has at its disposal a practically unlimited source of seawater for both feed and coolant (Fig. 3). Moreover, the simulated modules were based on an upscaled version of the device used in Figs. 2 and S2, and all parameters that are not specified are indicated in Table 1. Practical aspects or processes external to the module, such as solar resource availability and solar collector technology, go beyond the scope of this work and their effects are considered at the system boundaries (cf. Fig. 1b).

4.1. Modelled performance of a full-scale AGMD flat-sheet module

Fig. 4 shows the results from CFD simulations under steady state conditions, for salt water distillation of an aqueous solution with an inlet NaCl concentration of $c_{f,c,0}$ = 35 kg m^{-3}, using an AGMD module in the counter-current configuration depicted in Figs. 3a and 4a. As an illustration, Figs. 4a-e display the spatial distribution of variables describing the AGMD process using a module of length L = 1.5 m, of (F) and (C) thickness $\delta_{F,C}$ = 2 mm, with an (AG) thickness δ_{AG} = 4 mm, for a feed and coolant inflow average velocity $v_{f,c,0}$ = 1 cm s^{-1}, and for feed and coolant inlet temperatures $T_{in,f}$ = 50 °C and $T_{in,c}$ = 20 °C, respectively. Fig. 4a shows the temperature field throughout the module, where the highest and lowest temperature points correspond to $T_{in,f}$ and $T_{in,c}$ at the (F) and (C) channels inlet, respectively. As expected, $T(x,y)$ decreased along the direction of the feed flow and from the feed to the coolant due to the heat exchange through (M), (AG) and (CP). The temperature gradient between (F) and (C) drives the water evaporation from the feed and Fig. 4b evidences that the water partial pressure was indeed higher

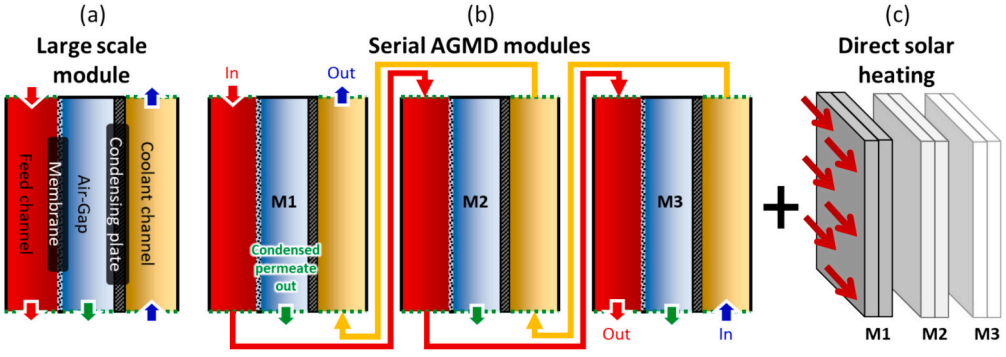
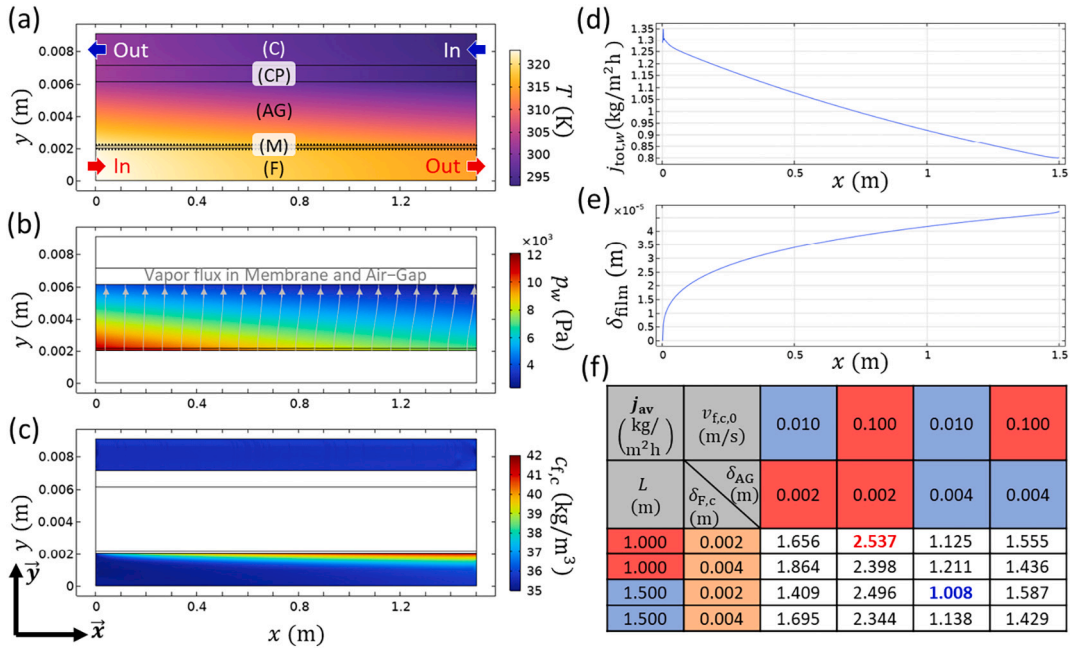


Fig. 3. Schematics of: (a) a single large scale AGMD module; (b) serially connected AGMD modules, (c) with an additional solar supply heating for the feed channel of the first module M1. In (a,b) the red and yellow arrows indicate respectively the feed and coolant circulation between the module channels. (c) The direct solar heating applied to the feed channel wall is effectively represented by an additional inlet diffusive heat flux along (F) wall. The coolant flow is considered to come from the same source as the feed saline solution.



j_{av} (kg/m^{2}h)	$v_{f,c,0}$ (m/s)	0.010	0.100	0.010	0.100
L (m)	$\delta_{F,c}$ (m) \ δ_{AG} (m)	0.002	0.002	0.004	0.004
1.000	0.002	1.656	2.537	1.125	1.555
1.000	0.004	1.864	2.398	1.211	1.436
1.500	0.002	1.409	2.496	1.008	1.587
1.500	0.004	1.695	2.344	1.138	1.429

Fig. 4. Simulated full-scale AGMD flat-sheet module: (a) temperature $T(x,y)$, (b) water partial pressure $p_w(x,y)$ in (M) and (AG), (c) salt distribution $c_{f,c}(x,y)$ in (F) and (C), (d) normal vapor flux at the (M/AG) interface $j_{tot,w}(x, \delta_F + \delta_M)$, and (e) condensate film thickness $\delta_{film}(x)$ predictions for $L = 1.5$ m, $\delta_{F,C} = 0.002$ m, $\delta_{AG} = 0.004$ m, and $v_{f,c,0} = 0.01$ m s^{-1}, and for feed and coolant inlet temperatures of $T_{in,f} = 50$ °C and $T_{in,c} = 20$ °C, respectively. (f) Predictions of the membrane-surface averaged steady-state permeate flux, j_{av} at (M/AG), for different values of L, $\delta_{F,C}$, δ_{AG}, and $v_{f,c,0}$. The rows are related to two different values of both L and $\delta_{F,C}$ (four combinations); the columns are related to two different values of both δ_{AG} and $v_{f,c,0}$ (four combinations), for a total number of sixteen predicted productivity values. The red boxes indicate parameter values that corresponded to higher j_{av} and, conversely, blue boxes indicate parameter values that led to a lower j_{av}; the orange boxes indicate the parameter whose influence j_{av} was not necessarily monotonic. The maximum and minimum value of j_{av} on the simulated range are indicated in red and blue fonts, respectively. The modules width is set at $W = 0.5$ m. The inlet feed and coolant salt density are set at $c_{f,c,0} = 35$ kg m^{-3}. All other parameters not indicated are given in Table 1.

in the membrane and at the inlet of the module where the temperature gradient was the steepest. Fig. 4b also plots the vapor flux direction, going from the (F/M) interface towards the cooled surface (CP) where the permeate condenses. The vapor flux direction deviated gradually from the membrane normal direction $(O, \vec{y})$ as the (AG) opening to external environment became closer (Fig. 4b), and the temperature and pressure gradient from the (AG) to the external environment drove an outflow of vapor. Consequently, the vapor flux entering the air-gap at the (M/AG) interface was slightly higher than that received by the condensate film at the (CP) surface, while a relatively small fraction of the vapor flux "escaped" from the module: from 0.3 %, up to 10 % of j_{av} for large AG opening (Fig. 4b). Fig. 4c shows that vaporization was accompanied with salt retention at (F/M) interface, feed side, which caused an increasingly thick and dense layer of brine to form along the feed flow, with the salt "layer thickness" (peak width) increasing from roughly 0.1 mm at $x = L/2$ to approximately 0.2 mm at $x = L$ (Fig. 4). Beside, Fig. 4c shows the salt concentration in the coolant, which was globally homogeneous and equal to $c_{f,c,0} = 35$ kg m^{-3} along (C), as no mass transfer occurred within. From inlet to outlet of the module, salt polarization in (F) combined with the temperature decrease in the vicinity of the (F/M) interface, lead to a decrease in the vapor pressure in the membrane (Fig. 4b), and thus a decrease in the (normal) vapor flux entering the air-gap, $j_{tot,w}$ (kg m^{-2} s^{-1}), defined by $j_{tot,w} = \overrightarrow{j_{tot,w}} \bullet \vec{y}$ (cf. **§2.2.2**), as depicted in Fig. 4d. Furthermore, Fig. 4e shows the spatial evolution of the condensate film thickness, whose spatial growth rate decreased as the film flow accelerated under gravity effect, and the received vapor flux decreased (Fig. 4d) from inlet to outlet of the module.

In line with literature reports [52], the AGMD production is first represented by j_{av} (kg m^{-2} h^{-1}), namely, the water permeate flux entering the (AG) normalized by the effective membrane surface area (Fig. 4f). The scenario described above (Figs. 4a-e) provided $j_{av} = 1.008$ (kg m^{-2} h^{-1}) (blue font value in Fig. 4f). In addition, Fig. S4 (SM-C) provides an estimation of the enthalpy variation in the feed solution between the inlet and outlet, which gives an indication about the thermal power consumption of the system for the tested configurations.

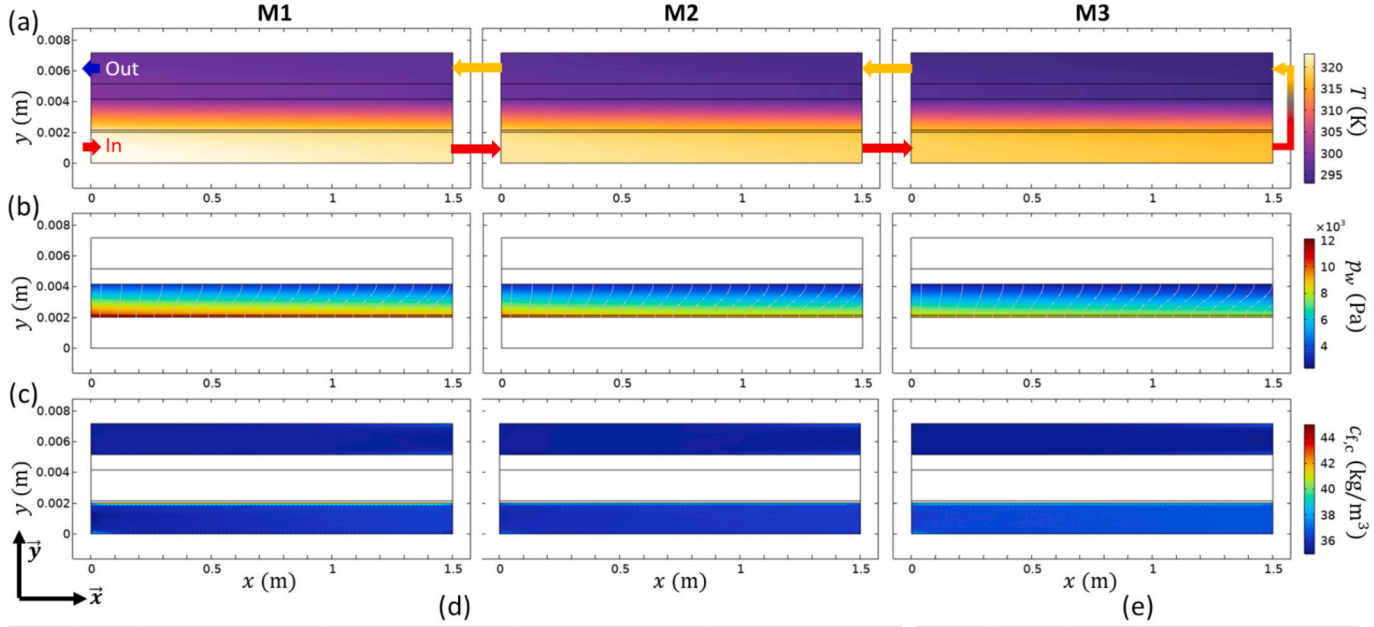
The CFD model then enabled to simulate different AGMD configurations by varying the module dimensions L, $\delta_{F,C}$, δ_{AG}, and operating condition $v_{f,c,0}$, for $T_{in,f} = 50$ °C and $T_{in,c} = 20$ °C. Calculated j_{av} values for each scenario are reported in Fig. 4f. For guidance, the parameter values chosen in Fig. 4f corresponded to a feed inflow characterized by a Reynolds number between 68 and 1350, a Sherwood number between 5.8 and 63, and a Nusselt number between 1.1 and 12.5, which corresponded to laminar flow conditions. As expected, the increase in $v_{f,c,0}$ led to higher j_{av}, as the mass flow rate and thus available thermal heating/cooling power increased. More importantly, the increase in δ_{AG} resulted in a considerable decrease of j_{av} for a fixed value of L, $\delta_{F,C}$, and $v_{f,c,0}$, which is explained by an increase in the air-gap thermal insulating role. Indeed, the spatial discretization of $T(x,y)$ and $p_w(x,y)$ in the membrane region illustrated in Figs. 4a and d, evidences that a greater distance between (CP) and (F/M) notably induced an increase of the temperature in the membrane region (cf. Fig. 4a), thereby reducing the driving force for vapor permeation through the membrane (cf. eqs. (10,14)). The increase of L also resulted in a decrease in the average permeate flux (Fig. 4f), mostly attributed to a more important heat exchange along the (F/M) interface (cf. Figs. 4a and d). However, this effect was minor, and overall, the permeate productivity of the AGMD module, i.e., the integral of the vapor flux multiplied by the membrane surface area, increased with the increase of the module length, for all other parameters fixed. The increase in the channels thickness $\delta_{F,C}$ decreased the (bulk) temperature variation within the feed and coolant, which resulted in an increase of j_{av} at low flow velocity values, i.e., conditions under which the convective heat transport was relatively low in (F) and (C).

Conversely, at higher $v_{f,c,0}$ values, the changes in $\delta_{F,C}$ had relatively low effect on j_{av}, which implies that the AGMD process, for a given flow velocity, can maintain its productivity and lower its power consumption (Fig. S4) by functioning with lower feed and coolant flow rates in narrower (F) and (C) channels, for all other parameters fixed.

In summary, Fig. 4 suggests that the optimal configuration for a full-scale module, combining a high permeate production rate and low power consumption for heating/cooling and flow circulation, is best achieved by opting for modules with long, thin channels and air-gap, and for high feed flow velocity values. It should be noted that that the air gap considered here is wide open at the outlet to facilitate condensate outflow and thus prevent flooding.

4.2. Modelled performance of full-scale AGMD modules in series

Fig. 5 reports the results of the simulations on the distillation of salt water using three AGMD modules connected in series in the configurations depicted in Figs. 3b and 5a, for different modules dimensions and inflow velocity. Figs. 5a-c display the temperature, vapor pressure, and salt distribution within a system of three connected modules, each with length $L = 1.5$ m, (F) and (C) thickness $\delta_{F,C} = 2$ mm, (AG) thickness $\delta_{AG} = 2$ mm, and a feed and coolant inflow velocity $v_{f,c,0} = 10$ cm s^{-1}. In the configuration illustrated in Fig. 3b, the same inlet flow velocity $v_{f,c,0}$ was imposed to each module feed and coolant inlet. Additionally, Fig. S5 provides an estimation of the thermal power consumed by the whole system, considering the feed temperature variation from inlet to outlet. In Fig. 5, the feed temperature and salt concentration were respectively $T_{in,f} = 50$ °C and $c_{f,0} = 35$ kg m^{-3} at module M1 feed inlet, and the successive modules were connected as follows: the feed salt concentration and temperature at M2 inlet were the average values of that at M1 feed outlet, and the same between M2 and M3. Oppositely, in counter-current configuration, the coolant temperature at module M3 coolant inlet was fixed at $T_{in,f} = 20$ °C in module M3 coolant inlet, then the temperature at M2 coolant inlet was the average value of that at M3 coolant outlet, and the same between M2 and M1. The cooling solution was assumed to come from the same source as the feed, with salt concentration $c_{c,0} = 35$ kg m^{-3} at M3 inlet that did not vary in the coolant stream from M3-M2-M1, as no mass transfer occurred in (C) (Fig. 5c). Hence, for each module taken individually, the variable gradient fields ($T(x,y)$, $p_w(x,y)$, and $c_{f,c}(x,y)$ in Figs. 5a-c) were similar to that described in Fig. 4. The simulation results indicate that the temperature field in (F) and (C) varied from M1 to M2 and M2 to M3 as (almost) if the three formed a single module, as a result of the counter-current configuration. Moreover, the temperature gradient throughout the modules was globally smaller than for a single module, e.g., the coolant temperature was higher in M1 than in Fig. 4a and, consequently, the



(d)

j_{av} (kg/m^{2}h)	$v_{f,c,0}$ (m/s)	0.010			0.100			0.010			0.100		
L (m)	$\delta_{F,C}$ (m) \ δ_{AG} (m)	0.002			0.002			0.004			0.004		
1.000	0.002	1.269	0.945	0.73	2.439	2.281	2.137	0.946	0.751	0.611	1.524	1.459	1.398
1.000	0.004	1.578	1.319	1.115	2.341	2.259	2.18	1.094	0.957	0.844	1.417	1.386	1.355
1.500	0.002	1.018	0.711	0.526	2.364	2.148	1.961	0.806	0.6	0.466	1.546	1.447	1.358
1.500	0.004	1.355	1.083	0.88	2.267	2.161	2.061	0.988	0.828	0.704	1.403	1.36	1.318

(e)

Q (kg/h)	$v_{f,c,0}$ (m/s)	0.010	0.100	0.010	0.100
L (m)	$\delta_{F,C}$ (m) \ δ_{AG} (m)	0.002	0.002	0.004	0.004
1.000	0.002	1.472	3.429	1.154	2.19
1.000	0.004	2.006	3.39	1.447	2.079
1.500	0.002	1.692	4.855	1.404	3.263
1.500	0.004	2.488	4.867	1.89	3.061

Fig. 5. Simulated full-scale AGMD system comprising three modules in series, M1, M2, and M3, as depicted in Fig. 3b. Specifically, simulated (a) temperature $T(x,y)$, (b) water partial pressure in (M) and (AG) $p_w(x,y)$, (c) salt distribution in (F) and (C) $c_{f,c}(x,y)$ for $L = 1.5$ m, $\delta_{F,C} = 0.002$ m, $\delta_{AG} = 0.002$ m, $v_{f,c,0} = 0.1$ m s^{-1}, and for feed and coolant inlet temperatures $T_{in,f} = 50$ °C and $T_{in,c} = 20$ °C, respectively. (d) Membrane-surface average vapor flux j_{av} in modules M1, M2 and M3 (three values of each cell, left to right), and (e) total permeate flux Q of the whole system, for feed inlet and coolant inlet temperatures of 50 °C and 20 °C, as function of L, $\delta_{F,C}$, $v_{f,c,0}$, and δ_{AG}. (d,e) The rows are related to two different values of both L and $\delta_{F,C}$ (four combinations); the columns are related to two different values of both δ_{AG} and $v_{f,c,0}$ (four combinations), for a total number of sixteen predicted productivity values. The red boxes indicate a parameter value that corresponded to higher j_{av} values and, conversely, blue boxes indicate parameter values that led to lower j_{av}; the orange boxes indicate the parameter whose influence was not necessarily monotonic. The maximum and minimum value of j_{av} on the simulated range are indicated in red and blue fonts, respectively. The modules width is set at $W = 0.5$ m. The inlet feed and coolant salt density are set at $c_{f,c,0} = 35$ kg m^{-3}. All other parameters not indicated are given in Table 1.

vapor pressure in (M) and (AG) was also lower, as shown in Fig. 5b. Of note is the fact that in Figs. 5a, the feed temperature decreased close to $T_{in,c}$ at M3 feed outlet.

Figs. 5d and e present, respectively, the membrane-surface average permeate flux in each module, j_{av}, and the corresponding overall permeate production rate Q (kg h^{-1}) for the entire system, i.e., the sum of the three j_{av} values multiplied by the active membrane area. For a given module dimension and set of operating conditions, j_{av} for M1 were sensibly lower than for a single module (Fig. 4f) and j_{av} decreased in M2 and M3, as a consequence of the decrease in the vapor permeation driving force, i.e., the temperature gradient in (M-AG-CP) (cf. Fig. 5a-c). The decrease in j_{av} between successive modules was more important for low feed inlet velocity (up to a 30 % drop between M1-M2-M3) than for high ones, such as in the scenario depicted in Figs. 5a-c, where j_{av} decreased 9 % between each connected module (Figs. 5d). This trend is due to a greater diffusive heat flux between the feed and coolant, resulting in a more important decrease (increase) in the feed (coolant) bulk temperature from inlet to outlet. As described in Fig. 4, the increase of $\delta_{F,C}$ reduced the heat loss and gain along the feed and coolant flow, respectively, which led to overall increase of the permeate flux, particularly at low $v_{f,c,0}$ values. For high convective flux in (F) and (C) the changes in $\delta_{F,C}$ had a smaller impact on j_{av} and particularly for a significant air-gap thickness value, e.g., the variation of j_{av} as function of $\delta_{F,C}$ are negligible for $\delta_{AG} = 0.004$ m, $v_{f,c,0} = 0.1$ m s^{-1}. These last examples also demonstrate that a thick air-gap ($\delta_{AG} = 0.004$ m) reduces the drop in j_{av} (below 5 % between connected modules), due to the thermal insulation effect generated by the (AG), thereby in these configurations, the air-gap should increase the thermal efficiency of the whole process (Fig. S5). Besides, the effect of the module length on the productivity of serial connected modules was comparable to that described in Fig. 4, and for thick (AG) the impact of L on j_{av} was also negligible.

Consequently, in terms of the productivity of the whole system (Fig. 5e), the highest Q values were reached for large values of $v_{f,c,0}$, L, and small δ_{AG} values, with a negligible impact of $\delta_{F,C}$ under these operating conditions, as expected from Fig. 4. The addition of a thicker air-gap significantly reduced permeate productivity for individual modules and for a three-module connected system. However, previous observations indicated that a relatively thick air-gap would likely allow more modules to be connected in series by limiting the effect of heat exchange between the feed and the coolant, i.e., feed heat loss and coolant heat gain. For high inlet velocities, additional coupling with thin (F) and (C) channels would further reduce the module thermal power consumption (Fig. S5) without impacting production (Figs. 5d and e), thus providing an efficient configuration with several connected modules. Conversely, for low inlet velocity, it should be preferable to use a thin air-gap coupled with thick channels (Fig. 5d, e and S5).

The results highlight clear design rules for maximizing performance in serial AGMD systems. First, feed and coolant velocity are the dominant lever: higher inflow rates sustain vapor flux in downstream modules by limiting thermal equilibration between feed and coolant. Second, air-gap thickness must be chosen carefully. A relatively thicker air-gap reduces individual module productivity but stabilizes performance through connected modules by insulating against rapid heat loss, allowing more units to be connected in series without severe flux decline. Third, increasing feed/coolant channel thickness enhances heat recovery and improves performance at low velocities, but has marginal benefit at high velocities. In summary, thin air-gaps and narrow channels at high flow rates maximize productivity per module, while thicker air-gaps and channels at lower velocities enable stable operation of multiple modules in train-like configurations.

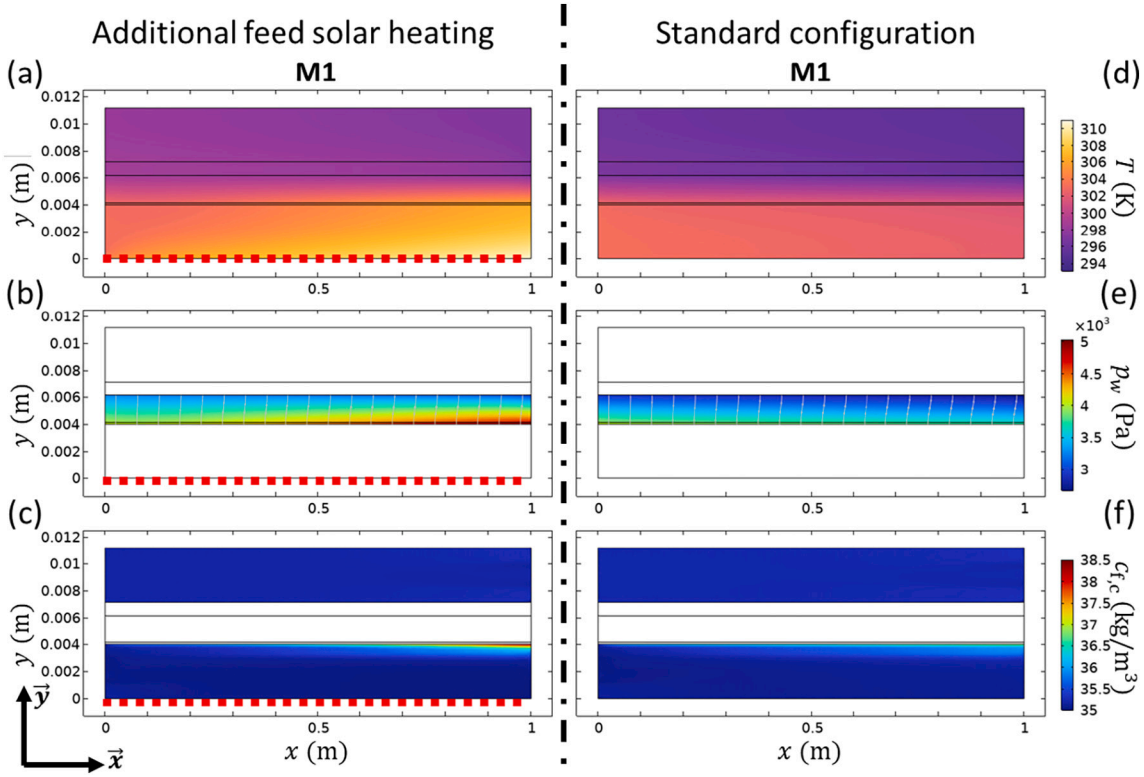


Fig. 6. Simulated AGMD module M1, part of the system of three modules in series: (a,d) temperature field $T(x,y)$, (b,e) water partial pressure field in (M) and (AG) $p_w(x,y)$, (c,f) salt distribution in (F) and (C) $c_{f,c}(x,y)$, for $L = 1$ m, $\delta_{F,C} = 0.004$ m, $\delta_{AG} = 0.002$ m, $v_{f,c,0} = 0.01$ m s^{-1}, and for feed and coolant inlet temperatures $T_{in,f} = 30$ °C and $T_{in,c} = 20$ °C, respectively. (a-c) System with and (d-f) without (standard configuration) an additional direct solar heating equivalent to 1000 W m^{-2} along the feed channel (red dotted line), according to the configuration depicted in Fig. 3c. The modules width is set at $W = 0.5$ m. The inlet feed and coolant salt density are set at $c_{f,c,0} = 35$ kg m^{-3}. All other parameters not indicated are given in Table 1.

4.3. Modelled performance of full-scale AGMD modules in series with direct solar irradiance

Figs. 6 and 7 present simulation results for an AGMD system comprising three modules in series, as described in Fig. 5 and considering an additional contribution of thermal power from direct solar heating of the feed solution, which was applied only on the first of the three modules (M1) (Fig. 3c). Effectively, a distributed diffusive heat source was considered along the feed channel wall of M1, located at $y = 0$ (Fig. 6a-c), with an intensity of 1000 W m^{-2}, assuming an optimal sun exposure [34,41,49,50]. Fig. 6 displays $T(x,y)$, $p_w(x,y)$, and $c_{f,c}(x,y)$ for module M1 only, characterized by $L = 1$ m, $\delta_{F,C} = 4$ mm and $\delta_{AG} = 2$ mm, under the operating conditions $v_{f,c,0} = 1$ cm s^{-1}, $c_{f,c,0} = 35$ kg m^{-3}, $T_{in,f} = 30$ °C and $T_{in,c} = 20$ °C, with (Fig. 6a-c) and without (Fig. 6d-f) solar power supply on M1. Furthermore, Fig. S6 provides an estimation of the thermal power consumed by the whole system, considering the inlet and outlet feed temperature difference, with (Fig. S6a) and without (Fig. S6b) the additional heat supply, which reduced enthalpy variation (negative values in Fig. S6a). In the standard situation where feed solution heating was assumed to be external to the system, Figs. 6d-f simply show lower temperature, partial pressure, salt concentration gradient and vapor flux values due to a lower feed inlet temperature, comparable to that in Figs. 5. With the direct solar heating, Fig. 6a shows that the lateral heat supply on module M1 generated a significant increase in the temperature (+10 °C) along the heating wall in (F), resulting in a higher feed temperature towards the channel outlet. Moreover, compared to the standard situation of Fig. 6d, the temperature was higher throughout the system, particularly in (F) and towards the membrane region, but also in the coolant, depending on the proximity to the lateral heat source in (F) and, more importantly, the flow velocity. At low flow rates, in module M1, lateral heating caused a significant increase in temperature in (F) which was relatively evenly distributed along the feed stream and, to a lesser extent, in the rest of the module, including the coolant (Fig. 6a), a negative setback on permeate productivity. The "enhanced" temperature gradient throughout the module M1 then generated a higher vapor flux at the bottom of the module (Fig. 6b compared to Fig. 6e) which in turn generated a thicker retained salt layer towards the feed channel outlet (Fig. 6c and f) and higher j_{av} values in M1 (Figs. 7a and 7b). At higher flow rates, the important convective flow reduced the heat stored by the feed along the (F) wall, which greatly diminished the benefit for permeation production in M1, while also reducing the heating of the coolant (cf. Fig. 6a). Consequently, comparing Figs. 7a to Fig. 7b, the j_{av} values in M1 were enhanced by additional direct solar heating for $v_{f,c,0} = 1$ cm s^{-1}, more than for $v_{f,c,0} = 10$ cm s^{-1}. Now regarding the modules downstream of the feed solution, the extra heat stored in M1 appeared to benefit the feed in M2 and M3, while the coolant in these modules was not directly affected by solar heating in the counterflow configuration. Fig. 7a indeed shows that j_{av} in M2 and M3 was higher than in M1 (unlike the standard configuration, cf. Fig. 5). In particular, as module M1 stores more heat at low inflow velocity, j_{av} in the downstream modules M2 and M3 was considerably higher than without solar enhancement (Fig. 7b). Conversely, the comparatively low amount of heat stored in M1 due to a higher feed flow rate had a limited impact on the permeate flux of the downstream modules (Figs. 7a and 7b). In addition, Figs. 7a highlights that a decrease in $\delta_{F,C}$ caused an increase in the heat stored by the feed in M1 as feed channel volume was smaller, which further increased j_{av} in M2 and M3. Meanwhile, (Fig. 7a) an increase in $\delta_{F,C}$ reduced the drop in j_{av} between M1 with solar heating and the subsequent modules by reducing the impact of the (F—C) heat exchange. In the same way, (Fig. 7a) the increase in δ_{AG} also balanced out the decrease in j_{av} in M1 due to the negative setback of direct solar heating, by insulating the coolant further away from lateral heating source in (F) (cf. Fig. 6a).

Regarding the overall permeate production of the tested configurations, the additional solar power supply in M1 (Fig. S6) clearly increased the permeate production rate Q, in particular for low $v_{f,c,0}$ values,

Additional feed solar heating

(a)

j_{av} (kg/m^{2}h)	$v_{f,c,0}$ (m/s)	0.010	0.100	0.010	0.100
L (m)	$\delta_{F,C}$ (m) \ δ_{AG} (m)	0.002	0.002	0.004	0.004
1.000	0.002	0.342 / 0.786 / 0.627	0.54 / 0.592 / 0.578	0.3 / 0.56 / 0.475	0.365 / 0.397 / 0.39
1.000	0.004	0.375 / 0.597 / 0.544	0.463 / 0.503 / 0.498	0.265 / 0.403 / 0.378	0.282 / **0.307** / **0.305**
1.500	0.002	**0.215** / **0.981** / **0.674**	**0.563** / 0.629 / 0.604	0.287 / 0.712 / 0.536	0.413 / 0.454 / 0.441
1.500	0.004	0.344 / 0.673 / 0.581	0.459 / 0.512 / 0.504	0.271 / 0.473 / 0.425	0.29 / 0.323 / 0.32

(c)

Solar enhancement* ←

Q (kg/h)	$v_{f,c,0}$ (m/s)	0.010	0.100	0.010	0.100
L (m)	$\delta_{F,C}$ (m) \ δ_{AG} (m)	0.002	0.002	0.004	0.004
1.000	0.002	0.877 +148 %	0.855 +11 %	0.668 +152 %	0.576 +10 %
1.000	0.004	0.758 +69 %	0.732 +6 %	0.523 +71 %	**0.447** +6 %
1.500	0.002	**1.402** +230 %	1.346 +16 %	1.151 +236 %	0.981 +13 %
1.500	0.004	1.198 +107 %	1.106 +9 %	0.877 +111 %	0.7 +8 %

Standard configuration

(b)

j_{av} (kg/m^{2}h)	$v_{f,c,0}$ (m/s)	0.010	0.100	0.010	0.100
L (m)	$\delta_{F,C}$ (m) \ δ_{AG} (m)	0.002	0.002	0.004	0.004
1.000	0.002	0.259 / 0.235 / 0.214	0.527 / 0.514 / **0.502**	0.19 / 0.177 / 0.164	0.356 / 0.35 / 0.345
1.000	0.004	0.316 / 0.299 / 0.284	0.464 / 0.459 / 0.454	0.212 / 0.204 / 0.197	0.283 / 0.281 / 0.279
1.500	0.002	0.215 / 0.187 / 0.165	**0.537** / **0.517** / 0.498	**0.169** / **0.152** / **0.137**	0.396 / 0.385 / 0.375
1.500	0.004	0.275 / 0.256 / 0.239	0.458 / 0.451 / 0.445	0.195 / 0.185 / 0.176	0.29 / 0.287 / 0.284

(d)

Q (kg/h)	$v_{f,c,0}$ (m/s)	0.010	0.100	0.010	0.100
L (m)	$\delta_{F,C}$ (m) \ δ_{AG} (m)	0.002	0.002	0.004	.004
1.000	0.002	0.354	0.772	**0.265**	0.525
1.000	0.004	0.449	0.689	0.307	0.421
1.500	0.002	0.425	**1.164**	0.343	0.867
1.500	0.004	0.578	1.016	0.416	0.645

Fig. 7. (a,b) Membrane-surface average vapor flux j_{av}, and (c,d) total permeate flux Q of a system comprising three modules in series (Fig. 3c), for a feed inlet and coolant inlet temperatures of 30 °C and 20 °C, as a function of L, $\delta_{F,C}$, $v_{f,c,0}$ and δ_{AG}, (a,c) with and (b,d) without (standard configuration) an additional direct solar heating equivalent to 1000 W m^{-2} along the feed channel. (a,b) Each cell reports the j_{av} values for the modules M1, M2, and M3, from left to right. (c,d) Each cell reports Q, the productivity of the entire system. The highest and lowest values of each table are reported in blue and red fonts, respectively. In (c), the percentage increase in productivity with solar enhancement compared to the standard configuration is shown (green). The modules width is set at $W = 0.5$ m. The inlet feed and coolant salt density are set at $c_{f,c,0} = 35$ kg m^{-3}. All other parameters not indicated are given in Table 1.

compared to the standard configuration. Then, it appears that Q was the highest when the increase in j_{av} from M1 to M2 was the steepest, for low inflow velocity and thin channels, i.e., when the solar heating in M1 likely served as a preheater for the downstream modules M2 and M3 (Figs. 7a). Consequently, in agreement with the literature [18], the solar enhancement effect was more significant at low flow rates, as the feed flow in M1 then absorbed more heat (Figs. 6a and S6a). Note that the production increase values for the specific scenarios detailed in Figs. 6 and 7 corresponded to optimal estimations of solar improvement based solely on the AGMD modules physics, and prior to addressing further practical considerations regarding collector technology and solar resource constraints for given environmental conditions.

In summary, adding a direct solar heater on the feed side can considerably improve the productivity of AGMD process, and especially in multistage systems when the excess heat absorbed by the upstream module is redistributed in the modules down the feed stream. The simulations showed that applying ~1000 W m^{-2} direct irradiation on the feed wall of the first module can raise the feed outlet temperature by ~10 °C, thus boosting flux in subsequent modules. To exploit this effect, system designers should: (i) operate at low to moderate feed velocities, which maximize heat uptake in the irradiated module; (ii) use thicker feed channels to increase heat storage capacity, ensuring that solar energy is carried downstream; (iii) adjust air-gap thickness to maintain cooling efficiency despite higher bulk feed temperatures. Feeding solar energy to each module could also further improve the permeate productivity of a system comprising modules in series, and in particular when operating at low feed speeds (cf. Fig. 7c). In this case, it would be advantageous, if not necessary, to increase the thickness of the feed channel and/or the thickness of the air-gap, so that the feed liquid could store as much heat as possible (cf. Fig. S6a) while maintaining high efficiency of the air-gap cooling.

5. Conclusion

In this work, the authors propose a new comprehensive formalism to describe the air-gap membrane distillation process on the basis of the Maxwell-Stefan theory for gas transport modified for the diffusion in porous membrane and accounting for medium vapor saturation. The theory is built on a general framework that enables to address the distillation process for different compositions of feed liquids, coolants, or stagnant gases in the air-gap, or to consider changes in the configuration of an AGMD system (e.g., component dimensions, connected modules). In this work, the model was refined and exemplified to address the specific case study of seawater desalination with and without enhancement by direct solar heating.

In particular, this work details the development of the formalism by focusing on the three physical aspects constituting the AGMD multiphysics, namely, the flow of a solution in contact with a porous medium, the transport of gas through the porous membrane and the air-gap, and the condensation of the permeate on a cooled surface. To grasp the complexity of diffusion phenomena in MD processes, the authors adopted the Maxwell-Stefan theory, which is modified to account for friction during diffusion of an air-water mixture in a porous medium, as well as water vapor saturation of the gaseous medium, based on considerations relating to the system entropy. The aforementioned physical aspects were combined into a complete formalism that describes heat and mass transfer at every location within an AGMD system. In order to evaluate the outcomes of this new formalism, the authors developed a CFD numerical model, which can simulate various AGMD processes with different module dimensions, as well as gas and liquid supply properties. Moreover, the validity of the numerical model's predictions was successfully validated with experimental results obtained on a laboratory-scale AGMD system.

As a relevant exemplification of the theoretical and numerical framework, the authors simulated the operation of full-scale AGMD modules, either individually or connected in series, to specifically predict their permeate production under steady-state conditions and to support effective designs by simulating different module characteristics and operating conditions, i.e., length and height of cooling and feed channels, membrane effective area, air-gap thickness, inlet flow velocities, and temperatures. The simulations indicated that: to increase the individual module efficiency, defined as productivity in relation to the energy consumed, it is preferable to opt for long modules with thin channels and a thin air-gap, working at high feed speed velocities. For a multistage AGMD system in train-like configuration with external heating of the feed solution, the overall efficiency of the system depends on the individual efficiency of the connected modules, but also on heat storage in the feed stream. Then, in serial configurations, the presence of a fully operational (thick) air-gap in AGMD modules limit the gradual loss of productivity from module to module, and so could improve the whole system efficiency. Finally, the authors looked at the benefits of adding solar heating to the feed liquid, by direct irradiation of the feed wall of a module. Simulations showed that this additional contribution can increase productivity, particularly at low feed rates, as long as the module is correctly dimensioned to maintain sufficient cooling of the air-gap. In a system comprising modules in series, solar enhancement of an upstream module greatly increases the efficiency of downstream modules, by transmitting stored solar energy. Importantly, the simulations also highlighted that no straightforward quantitative correlation can be established between the variation in the values of the tested parameters and their impact on the productivity of the modules, whether a single one or multiple ones connected in series, depending on operating conditions and for a given membrane.

A key contribution of this work is to provide a comprehensive multiphysics model that can be used to predict the optimal performance of an AGMD module, prior to further development of the design and implementation of real AGMD systems. Unlike simplified analytical models, the fully discretized CFD approach enables accurate scaling from laboratory modules to pilot and industrial systems. This makes it suitable as a 'digital twin' of AGMD modules, supporting decision-making in module sizing, system configuration, and integration with renewable energy sources. Thus, the model helps reduce reliance on costly experimental prototyping and accelerates the translation of AGMD into viable desalination technologies. In fact, the scenarios explored in this study constituted a non-exhaustive list of configurations that can be explored using the model developed in this work. The CFD-based multiphysics framework can straightforwardly be applied to other issues where AGMD is relevant, such as alcohol/water separation [95], and also consider transient phenomena, such as time variations in the availability of solar resources in a given environment [50]. The theory can also be expanded by addressing its limitations, e.g., by accounting for the wettability of the membrane as function of the properties of the liquid-gas phases in presence [93]. Furthermore, the formalism can be further complexified in order to integrate innovative AGMD techniques, e.g., the use of a superhydrophobic condensing plate to enhance permeate recovery [96]. All these considerations should be integrated in a consistent way into the multiphysics framework which is intended to serve as a basis for a physical study of AGMD processes.

Nomenclature

Abbreviations

AGMD	Air-Gap Membrane distillation
AG	Air-Gap
C	Coolant channel
CP	Condensing Plate
F	Feed channel
M	Membrane

Latin

c_c, c_f	Mass densities of salt in feed and coolant, respectively (kg m^{-3})
$c_{c,0}$, $c_{f,0}$,	Inlet salt densities in (C) and (F) channels respectively (kg m^{-3})
$\overline{c}_g$	Molar concentration of the gas phase (mol m^{-3})
$C_{p,c}$, $C_{p,f}$, $C_{p,g}$, $C_{p,m}$, $C_{p,M}$, $C_{p,s}$	Heat capacities of the coolant, feed, gas phase, membrane material, membrane with gas inclusion, and seawater type solution (Eq.(S2)), respectively (J kg^{-1} K^{-1})
$\overrightarrow{d_i}$	Diffusion driving force (Eq.(10)) (m^{-1})
D_c, D_f, D_s	Diffusion coefficients of a solute (salt) in the coolant, feed and seawater type solution (Eq.(S7)), respectively (m^2 s^{-1})
$D_{w,a}$	Maxwell-Stefan diffusion coefficient for water and air gas mixture (Eq.(15)), (m^2 s^{-1})
$\widehat{D}_{k,i}$, $\widehat{D}_{w,a}$	Fick multicomponent diffusion coefficients for the gas pair (k,i), and for water and air (w,a) (m^2 s^{-1})
D_i^K, D_a^K, D_w^K,	Knudsen diffusion coefficients of the species i, air and water (Eq.(12)), respectively (m^2 s^{-1})
$\overrightarrow{g}$	Gravitational acceleration vector (m s^{-2})
$\overrightarrow{g_i}$	External constraint exerted on the species i during diffusion (Eq.(11)) (m s^{-2})
$\overrightarrow{j_{c,i}}$, $\overrightarrow{j_{d,i}}$, $\overrightarrow{j_{tot,i}}$	Convective, diffusive and total mass flux of the species i, respectively (kg m^{-2} s^{-1})
j_{av}	Vapor mass flux at the M/AG interface, averaged over the effective membrane area (kg m^{-2} h^{-1})
k_c, k_f, k_g, k_m, k_M, k_s	Thermal conductivities of the coolant, feed, gas phase, membrane material, porous membrane (Eq.(1)), and seawater type solution (Eq.(S3)), respectively (W m^{-1} K^{-1})
L	Module length (m)
M_i, M_a, M_w	Molar weights of the species i, air and water, respectively (kg m^{-3})
p	Absolute pressure (Pa)
p_i, $p_{sat,i}$	Partial pressure and saturation pressure of species i (Pa)
Q	Total permeate mass flux (kg h^{-1})
r_M	Membrane pore radius (m)
R	Gaz constant (J mol^{-1} K^{-1})
T	Absolute temperature (K)
$T_{in,c}$, $T_{in,f}$	Absolute temperature at (C) and (F) inlet respectively (K)
$\overrightarrow{u}$	Velocity vector of the gas phase in (M-AG) (m s^{-1})
$\overrightarrow{v}$	Velocity vector of the feed and coolant solution (m s^{-1})
$v_{c,0}$, $v_{f,0}$	Inlet flow velocities in (C) and (F) channels respectively (m s^{-1})
W	Module width (m)
x_i, x_a, x_w, $x_{sat,w}$	Molar fractions of the species i, air and water in the gas phase, and molar fraction of saturated water vapor, respectively
x	Abscissa position (Fig. 1) (m)
y	Ordinate position (Fig. 1) (m)

Greek

α_c, α_f, α_g α_M, α_s	Heat diffusivity coefficients of coolant, feed, gas phase, membrane and seawater type solution, respectively (m^2 s^{-1})
δ_{AG}, δ_C, δ_{CP}, δ_F, δ_{film}, δ_M	Thicknesses of the air-gap, coolant channel, condensing plate, condensate film (Eq.(16)), feed channel, and membrane, respectively (m)
ε_M	Membrane porosity
κ	Membrane permeability to convective flow (m^2)
μ_c, μ_f, μ_{film}, μ_g, μ_s	Viscosities of the coolant, feed, condensate film, gas phase, and seawater type solution (Eq.(S4)), respectively (Pa s)
ρ_c, ρ_f, ρ_{film}, ρ_g, ρ_m, ρ_M, ρ_s	Mass concentrations of the coolant, feed, condensate film, gas phase, membrane material, membrane with gas inclusion, and seawater type solution (Eq.(S1)), respectively (kg m^{-3})
τ_M	Membrane pore tortuosity
ω_i, ω_a, ω_w	Mass fractions of the species i, air and water in the gas phase

CRediT authorship contribution statement

Nicolas Lesniewska: Writing – original draft, Visualization, Validation, Software, Methodology, Investigation, Formal analysis, Conceptualization. **Matteo Morciano:** Writing – review & editing, Supervision, Methodology, Conceptualization. **Alberto Tiraferri:** Writing – review & editing, Supervision, Resources, Project administration, Funding acquisition. **Matteo Fasano:** Writing – review & editing, Supervision, Resources, Project administration, Funding acquisition, Conceptualization.

Declaration of competing interest

The authors declare the following financial interests/personal relationships which may be considered as potential competing interests: Matteo Fasano and Alberto Tiraferri report financial support was provided by European Commission. If there are other authors, they declare that they have no known competing financial interests or personal relationships that could have appeared to influence the work reported in this paper.

Acknowledgements

This work was funded by the European Union Horizon Europe Research and Innovation Programme under grant agreement number 101091915 (acronym "MEloDIZER"). Views and opinions expressed are however those of the author(s) only and do not necessarily reflect those of the European Union or the European Health and Digital Executive Agency (HADEA). Neither the European Union nor the granting authority can be held responsible for them. M.M., M.F. and A.T. thank the CleanWaterCenter@PoliTo.

Appendix A. Supplementary data

Supplementary data to this article can be found online at https://doi.org/10.1016/j.desal.2025.119700.

Data availability

Data will be made available on request.

References

[1] M.M. Mekonnen, A.Y. Hoekstra, Sustainability: four billion people facing severe water scarcity, Sci. Adv. 2 (2016), https://doi.org/10.1126/sciadv.1500323.
[2] C. He, Z. Liu, J. Wu, X. Pan, Z. Fang, J. Li, B.A. Bryan, Future global urban water scarcity and potential solutions, Nat. Commun. 12 (2021), https://doi.org/10.1038/s41467-021-25026-3.
[3] A. Abdelfattah, S.S. Ali, H. Ramadan, E.I. El-Aswar, R. Eltawab, S.H. Ho, T. Elsamahy, S. Li, M.M. El-Sheekh, M. Schagerl, M. Kornaros, J. Sun, Microalgae-based wastewater treatment: mechanisms, challenges, recent advances, and future prospects, Environ. Sci. Ecotechnol. 13 (2023) 100205, https://doi.org/10.1016/j.ese.2022.100205.
[4] N.S. Robins, J. Fergusson, Groundwater scarcity and conflict – managing hotspots, Earth Perspect. 1 (2014) 6, https://doi.org/10.1186/2194-6434-1-6.
[5] E. Kellner, The controversial debate on the role of water reservoirs in reducing water scarcity, WIREs Water 8 (2021), https://doi.org/10.1002/wat2.1514.
[6] H. Shemer, S. Wald, R. Semiat, Challenges and solutions for global water scarcity, Membranes (Basel) 13 (2023), https://doi.org/10.3390/membranes13060612.
[7] A.N. Angelakis, M. Valipour, K.H. Choo, A.T. Ahmed, A. Baba, R. Kumar, G.S. Toor, Z. Wang, Desalination: from ancient to present and future, Water (Basel) 13 (2021), https://doi.org/10.3390/w13162222.
[8] J. Wang, E. Huo, Opportunities and challenges of seawater desalination technology, Front. Energy Res. 10 (2022), https://doi.org/10.3389/fenrg.2022.960537.
[9] N.R. Dalezios, A.N. Angelakis, S. Saeid Eslamian, Water scarcity management: part 1: methodological framework, Int. J. Global Environmental Issues 17 (2018), https://doi.org/10.1504/IJGENVI.2018.090629.
[10] S.A. Kalogirou, Seawater desalination using renewable energy sources, Prog. Energy Combust. Sci. 31 (2005) 242–281, https://doi.org/10.1016/j.pecs.2005.03.001.
[11] M. Elimelech, W.A. Phillip, The future of seawater desalination: energy, technology, and the environment, Science (AAAS) 333 (2011) 712–717, https://doi.org/10.1126/science.1200488.
[12] G. Amy, N. Ghaffour, Z. Li, L. Francis, R.V. Linares, T. Missimer, S. Lattemann, Membrane-based seawater desalination: present and future prospects, Desalination 401 (2017) 16–21, https://doi.org/10.1016/j.desal.2016.10.002.
[13] J. Bear, Dynamics of Fluids in Porous Media, Dover Publications, Inc., New York, 1972.
[14] A.-S. Jonsson, R. Wimmerstedt, A.-C. Harrysson, Membrane distillation - A theoretical study of evaporation through microporous membranes, Desalination 56 (1985) 237–249, https://doi.org/10.1016/0011-9164(85)85028-1.

[15] M. Giagnorio, M. Morciano, W. Zhang, C. Hélix-Nielsen, M. Fasano, A. Tiraferri, Coupling of forward osmosis with desalination technologies: system-scale analysis at the water-energy nexus, Desalination 543 (2022), https://doi.org/10.1016/j.desal.2022.116083.
[16] A. Naeimi Tabasian, F. Ricceri, M. Morciano, G. Boscheri, R. Perelli, M. Fasano, A. Tiraferri, Modeling and experimental evaluation of membrane distillation aimed at urine treatment for direct potable reuse in space stations, Desalination 572 (2024), https://doi.org/10.1016/j.desal.2023.117119.
[17] M. Morciano, M. Malaguti, F. Ricceri, A. Tiraferri, M. Fasano, Process optimization of osmotic membrane distillation for the extraction of valuable resources from water streams, NPJ Clean Water 7 (2024), https://doi.org/10.1038/s41545-023-00294-2.
[18] R.R. Meo, L. Craveri, E. Bertozzi, M. Malaguti, A. Tiraferri, M. Morciano, M. Fasano, Systematic exploration of direct solar absorption potential to enhance direct contact membrane distillation, Desalination 606 (2025), https://doi.org/10.1016/j.desal.2025.118740.
[19] T. Peters, Membrane technology for water treatment, Chem. Eng. Technol. 33 (2010) 1233–1240, https://doi.org/10.1002/ceat.201000139.
[20] A. Yusuf, A. Sodiq, A. Giwa, J. Eke, O. Pikuda, G. De Luca, J.L. Di Salvo, S. Chakraborty, A review of emerging trends in membrane science and technology for sustainable water treatment, J. Clean. Prod. 266 (2020), https://doi.org/10.1016/j.jclepro.2020.121867.
[21] E. Findley, Vaporization through porous membranes, Ind. Eng. Chem. Process. Des. Dev. 6 (1967) 226–230, https://doi.org/10.1021/i260022a013.
[22] H. Strathmann, Membrane separation processes, J. Membr. Sci. 9 (1981) 121–189.
[23] S. Kimura, S.-I. Nakao, Transport phenomena in membrane distillation, J. Membr. Sci. 33 (1987) 285–298.
[24] K. Smolders, A.C.M. Franken, Terminology for membrane distillation, Desalination 72 (1989) 249–262.
[25] V.T. Shahu, S.B. Thombre, Air gap membrane distillation: A review, J. Renew. Sustain. Energy 11 (2019), https://doi.org/10.1063/1.5063766.
[26] S. Noamani, S. Niroomand, M. Rastgar, M. Azhdarzadeh, M. Sadrzadeh, Modeling of air-gap membrane distillation and comparative study with direct contact membrane distillation, Ind. Eng. Chem. Res. 59 (2020) 21930–21947, https://doi.org/10.1021/acs.iecr.0c04464.
[27] E. Chiavazzo, M. Morciano, F. Viglino, M. Fasano, P. Asinari, Transport analysis of air-gap membrane distillation, J. Membr. Sci. 255 (2005) 239–253, https://doi.org/10.1016/j.memsci.2005.01.038.
[28] C.M. Guijt, G.W. Meindersma, T. Reith, A.B. De Haan, Air gap membrane distillation: 1. Modelling and mass transport properties for hollow fibre membranes, Sep. Purif. Technol. 43 (2005) 233–244, https://doi.org/10.1016/j.seppur.2004.09.015.
[29] A. Alkhudhiri, N. Darwish, N. Hilal, Membrane distillation: A comprehensive review, Desalination 287 (2012) 2–18, https://doi.org/10.1016/j.desal.2011.08.027.
[30] A.S. Alsaadi, N. Ghaffour, J.D. Li, S. Gray, L. Francis, H. Maab, G.L. Amy, Modeling of air-gap membrane distillation process: A theoretical and experimental study, J. Membr. Sci. 445 (2013) 53–65, https://doi.org/10.1016/j.memsci.2013.05.049.
[31] H. Al-Zoubi, F. Al-Amri, A.E. Khalifa, A. Al-Zoubi, M. Abid, E. Younis, T.K. Mallick, A comprehensive review of air gap membrane distillation process, Desalin. Water Treat. 110 (2018) 27–64, https://doi.org/10.5004/dwt.2018.22184.
[32] J. Choi, J. Cho, H. Cha, K.G. Song, Computational fluid dynamics simulation of the stacked module in air gap membrane distillation for enhanced permeate flux and energy efficiency, Appl. Energy 360 (2024), https://doi.org/10.1016/j.apenergy.2024.122805.
[33] H.C. Duong, P. Cooper, B. Nelemans, T.Y. Cath, L.D. Nghiem, Evaluating energy consumption of air gap membrane distillation for seawater desalination at pilot scale level, Sep. Purif. Technol. 166 (2016) 55–62, https://doi.org/10.1016/j.seppur.2016.04.014.
[34] E. Chiavazzo, M. Morciano, F. Viglino, M. Fasano, P. Asinari, Passive solar high-yield seawater desalination by modular and low-cost distillation, Nat. Sustainability 1 (2018) 763–772, https://doi.org/10.1038/s41893-018-0186-x.
[35] W.F. Blatt, A. Dravid, A.S. Michaels, U. Nelsen, Solute polarization and cake formation in membrane ultrafiltration causes consequences and control techniques, Membr. Sci. Technol. (1970) 47–97, https://doi.org/10.1007/978-1-4684-1851-4_4.
[36] L. Song, M. Eiimelech, Theory of concentration polarization in crossflow filtration, J. Chem. Soc. Faraday Trans. 91 (1995) 3389–3398, https://doi.org/10.1039/FT9959103389.
[37] M.H. Somerville, Non-isothermal Gaseous Flow through Fine Pored Media, 1972.
[38] F. Gao, X.C. Chen, G. Yu, C. Asumana, Compressible gases transport through porous membrane: A modified dusty gas model, J. Membr. Sci. 379 (2011) 200–206, https://doi.org/10.1016/j.memsci.2011.05.064.
[39] E.M. Sparrow, J.L. Gregg, A boundary-layer treatment of laminar-film condensation, J. Heat Transf. 81 (1959) 13–18, https://doi.org/10.1115/1.4008118.
[40] B. El Fil, G. Kini, S. Garimella, A review of dropwise condensation: theory, modeling, experiments, and applications, Int. J. Heat Mass Transf. 160 (2020) 120172, https://doi.org/10.1016/j.ijheatmasstransfer.2020.120172.
[41] M. Boukhriss, K. Zhani, R. Ghribi, Study of thermophysical properties of a solar desalination system using solar energy, desalination, Desalin. Water Treat. 51 (2013) 1290–1295, https://doi.org/10.1080/19443994.2012.714925.
[42] S. Kim, K.J. Kim, Dropwise condensation modeling suitable for superhydrophobic surfaces, J. Heat Transf. 133 (2011), https://doi.org/10.1115/1.4003742.
[43] R. Baghel, S. Kalla, S. Upadhyaya, S.P. Chaurasia, K. Singh, CFD modeling of vacuum membrane distillation for removal of Naphthol blue black dye from aqueous solution using COMSOL multiphysics, Chem. Eng. Res. Des. 158 (2020) 77–88, https://doi.org/10.1016/j.cherd.2020.03.016.
[44] J. Alonso, L. Martinelli, A. Jameson, Multigrid Unsteady Navier-Stokes Calculations with Aeroelastic Applications, 33rd Aerospace Sciences Meeting and Exhibit, 1995, https://doi.org/10.2514/6.1995-48.
[45] M. Mulder, Basic Principles of Membrane Technology, Springer Netherlands, Dordrecht, 1996, https://doi.org/10.1007/978-94-009-1766-8.
[46] M.A. Rahman, M.Z. Saghir, Thermodiffusion or Soret effect: historical review, Int. J. Heat Mass Transf. 73 (2014) 693–705, https://doi.org/10.1016/j.ijheatmasstransfer.2014.02.057.
[47] F. Kapteijn, J.A. Moulijn, R. Krishna, The generalized Maxwell-Stefan model for diffusion in zeolites: sorbate molecules with different saturation loadings, Chem. Eng. Sci. 55 (2000) 2923–2930, https://doi.org/10.1016/S0009-2509(99)00564-3.
[48] A.E. Khalifa, S.M. Alawad, Air gap and water gap multistage membrane distillation for water desalination, Desalination 437 (2018) 175–183, https://doi.org/10.1016/j.desal.2018.03.012.
[49] E.K. Summers, J.H. Lienhard, Experimental study of thermal performance in air gap membrane distillation systems, including the direct solar heating of membranes, Desalination 330 (2013) 100–111, https://doi.org/10.1016/j.desal.2013.09.023.
[50] M. Boukhriss, H. Ben Bacha, The performance of an AGMD unit coupled with a water solar collector the experimental validation for desalination of seawater, J. Fundam. Renew. Energy Appl. 08 (2018), https://doi.org/10.4172/2090-4541.1000257.
[51] E. Guillén-Burrieza, D.C. Alarcón-Padilla, P. Palenzuela, G. Zaragoza, Techno-economic assessment of a pilot-scale plant for solar desalination based on existing plate and frame MD technology, Desalination 374 (2015) 70–80, https://doi.org/10.1016/j.desal.2015.07.014.
[52] D. Winter, Membrane Distillation : A Thermodynamic, Technological and Economic Analysis, 2015.
[53] R.B. Bird, W.E. Stewart, E.N. Lightfoot, Transport Phenomena, 2 Nd, Wiley, 2002.
[54] C.F. Curtiss, R. Byron Bird, Multicomponent diffusion, Ind. Eng. Chem. Res. 38 (1999) 2515–2522, https://doi.org/10.1021/ie9901123.
[55] W.H. Emerson, D.T. Jamieson, Some physical properties of sea water in various concentrations, Desalination 3 (1967) 213–224, https://doi.org/10.1016/0011-9164(67)80012-2.
[56] B.M. Fabuss, A. Korosi, D.F. Othmer, Viscosities of aqueous solutions of several electrolytes present in sea water, J. Chem. Eng. Data 14 (1969) 192–197, https://doi.org/10.1021/je60041a025.
[57] D.T. Jamieson, J.S. Tudhope, R. Morris, G. Cartwright, Physical properties of sea water solutions: heat capacity, Desalination 7 (1969) 23–30, https://doi.org/10.1016/S0011-9164(00)80271-4.
[58] D.T. Jamieson, J.S. Tudhope, Physical properties of sea water solutions: thermal conductivity, Desalination 8 (1970) 393–401, https://doi.org/10.1016/S0011-9164(00)80240-4.
[59] J.D. Isdale, C.M. Spence, J.S. Tudhope, Physical properties of sea water solutions: viscosity, Desalination 10 (1972) 319–328, https://doi.org/10.1016/S0011-9164(00)80002-8.
[60] J.D. Isdale, R. Morris, Physical properties of sea water solutions: density, Desalination 10 (1972) 329–339, https://doi.org/10.1016/S0011-9164(00)80003-X.
[61] M.H. Sharqawy, J.H. Lienhard V, S.M. Zubair, Thermophysical properties of seawater: A review of existing correlations and data, desalination, Desalin. Water Treat. 16 (2010) 354–380, https://doi.org/10.5004/dwt.2010.1079.
[62] K.G. Nayar, M.H. Sharqawy, L.D. Banchik, J.H. Lienhard, Thermophysical properties of seawater: A review and new correlations that include pressure dependence, Desalination 390 (2016) 1–24, https://doi.org/10.1016/j.desal.2016.02.024.
[63] M. Sheikh, A. Fassadi Chimeh, F. Zokaee Ashtiani, A. Fouladitajar, Mathematical modeling of direct contact membrane distillation (DCMD) using Knudsen-diffusion model for PVDF membranes, J. Membr. Sci. Res. 11 (2025) 2040777, https://doi.org/10.22079/jmsr.2025.2040777.1676.
[64] W. Sobieski, S. Lipiński, The analysis of the relations between porosity and tortuosity in granular beds, Technical Sciences 20 (2017) 75–85, https://doi.org/10.31648/ts.2912.
[65] M.C. García-Payo, M.A. Izquierdo-Gil, Thermal resistance technique for measuring the thermal conductivity of thin microporous membranes, J. Phys. D. Appl. Phys. 37 (2004) 3008–3016, https://doi.org/10.1088/0022-3727/37/21/011.
[66] E.E. Gonzo, Estimating correlations for the effective thermal conductivity of granular materials, Chem. Eng. J. 90 (2002) 299–302.
[67] L.I. Stiel, G. Thodos, The thermal conductivity of nonpolar substances in the dense gaseous and liquid regions, AICHE J. 10 (1964), https://doi.org/10.1002/aic.690100114.
[68] K.W. Lawson, D.R. Lloyd, Membrane distillation, J. Membr. Sci. 124 (1997) 1–25.
[69] R.W. Schofield, A.G. Fane, C.J.D. Fell, Heat and mass transfer in membrane distillation, J. Membr. Sci. 33 (1987) 299–313.
[70] C.R. Wilke, P. Chang, Correlation of diffusion coefficients in dilute solutions, AICHE J. 1 (1955) 264–270, https://doi.org/10.1002/aic.690010222.
[71] E.A. Mason, A.P. Malinauskas, R.B. Evans, Flow and diffusion of gases in porous media, J. Chem. Phys. 46 (1967) 3199–3216, https://doi.org/10.1063/1.1841191.
[72] R.S. Brokaw, Viscosity of Gas Mixtures, NASA Technical Note, 1968.
[73] R.E. Cunningham, R.J.J. Williams, Diffusion in Gases and Porous Media, Springer New York, NY, 1980, https://doi.org/10.1007/978-1-4757-4983-0.

[74] H. Jiang, A.P. Straub, V. Karanikola, Ammonia recovery with sweeping gas membrane distillation: energy and removal efficiency analysis, ACS ES&T Eng. 2 (2022) 617–628, https://doi.org/10.1021/acsestengg.1c00294.
[75] J.C. Maxwell M.A. II, Illustrations of the dynamical theory of gases, Lond. Edinb. Dubl. Phil. Mag 20 (1860) 21–37.
[76] R. Krishna, J.A. Wesselingh, The Maxwell-Stefan approach to mass tranfer, Chem. Eng. Sci. 52 (1997) 861–911, https://doi.org/10.1016/S0009-2509(96)00458-7.
[77] E.A. Mason, R.B. Evans, G.M. Watson, Gaseous diffusion in porous media. III. Thermal transpiration, J. Chem. Phys. 38 (1963) 1808–1826, https://doi.org/10.1063/1.1733880.
[78] J.M. Kincaid, E.G.D. Cohen, M. López De Haro, The Enskog theory for multicomponent mixtures. IV. Thermal diffusion, J. Chem. Phys. 86 (1986) 963–975, https://doi.org/10.1063/1.452243.
[79] E.P. Bartlett, R.M. Kendall, R.A. Rindal, A unified approximation for mixture transport properties for multicomponent boundary-layer applications, NASA Technical Reports Server Part IV (1968) 1–42.
[80] R.B. Bird, D.J. Klingenberg, Multicomponent diffusion-A brief review, Adv. Water Resour. 62 (2013) 238–242, https://doi.org/10.1016/j.advwatres.2013.05.010.
[81] H. Ekström, Combining wall interactions, fluid momentum balances and the Maxwell-Stefan equations for gas transport in porous media: an alternative approach, Int. J. Thermofluids 21 (2024), https://doi.org/10.1016/j.ijft.2023.100534.
[82] M. Knudsen, Die Gesetze der Molekularströmung und der inneren Reibungsströmung der Gase durch Röhren, Ann. Phys. 333 (1909) 75–130, https://doi.org/10.1002/andp.19093330106.
[83] J.B. Young, B. Todd, Modelling of multi-component gas flows in capillaries and porous solids, Int. J. Heat Mass Transf. 48 (2005) 5338–5353, https://doi.org/10.1016/j.ijheatmasstransfer.2005.07.034.
[84] W.L. Brown, Entropie de configuration, solution solide et structure cristalline, Bull. Soc. Fr. Minéral. Cristallogr. 94 (1971) 38–44, https://doi.org/10.3406/bulmi.1971.6548.
[85] S. Sugawara, I. Michiyoshi, Dropwise Condensation, 1956.
[86] H.R. Nagendra, M.A. Tirunarayanan, Laminar film condensation from nonisothermal vertical flat plates, Chem. Eng. Sci. 25 (1970) 1073–1079.
[87] J.H. Lienhard, V.K. Dhir, Laminar film condensation on nonisothermal and arbitrary-heat-flux surfaces, and on fins, J. Heat Transf. 96 (1974) 197–203, https://doi.org/10.1115/1.3450164.
[88] H.J.H. Brouwers, Film condensation on non-isothermal vertical plates, Int. J. Heat Mass Transf. 32 (1989) 655–663, https://doi.org/10.1016/0017-9310(89)90213-5.
[89] H.J.H. Brouwers, Pure steam condensation experiments on nonisothermal vertical plates, J Heat Trans-T ASME 114 (1992) 714–718, http://www.asme.org/about-.
[90] D.M. Warsinger, J. Swaminathan, L.L. Morales, J.H. Lienhard V, Comprehensive condensation flow regimes in air gap membrane distillation: visualization and energy efficiency, J. Membr. Sci. 555 (2018) 517–528, https://doi.org/10.1016/j.memsci.2018.03.053.
[91] J.R.A. Pearson, A note on the "Danckwerts" boundary conditions for continuous flow reactors, Chem. Eng. Sci. 10 (1959) 281–284.
[92] M.C. Porter, Concentration polarization with membrane ultrafiltration, Ind. Eng. Chem. Res. 11 (1972) 234–248, https://doi.org/10.1021/i360043a002.
[93] D. Shi, T. Gong, W. Qing, X. Li, S. Shao, Unique behaviors and mechanism of highly soluble salt-induced wetting in membrane distillation, Environ. Sci. Technol. 56 (2022) 14788–14796, https://doi.org/10.1021/acs.est.2c03348.
[94] S.G. Joshi, A.E. Childress, A.L. McGaughey, Onset, rate, and depth of wetting front progression in membrane distillation, J. Membr. Sci. 713 (2025) 123253, https://doi.org/10.1016/j.memsci.2024.123253.
[95] V. Soni, J. Abildskov, G. Jonsson, R. Gani, Modeling and analysis of vacuum membrane distillation for the recovery of volatile aroma compounds from black currant juice, J. Membr. Sci. 320 (2008) 442–455, https://doi.org/10.1016/j.memsci.2008.04.025.
[96] B. Peng, X. Ma, Z. Lan, W. Xu, R. Wen, Analysis of condensation heat transfer enhancement with dropwise-filmwise hybrid surface: droplet sizes effect, Int. J. Heat Mass Transf. 77 (2014) 785–794, https://doi.org/10.1016/j.ijheatmasstransfer.2014.05.052.